



Analysis of Andreas Mogensen's moon images: a DTU Bachelor's Thesis

Danmarks Meteorologiske Institut

DMI Rapport 24 13
September 2024

af Mathilde Saltoft Schou.



Danmarks Meteorologiske Institut



Kolofon

Serietitel	DMI-rapport
Titel	Analysis of Andreas Mogensen's moon images: a DTU Bachelor's Thesis
Undertitel	
Forfatter(e)	Mathilde Saltoft Schou.
Andre bidragsydere	
Ansvarlig institution	Danmarks Meteorologiske Institut
Sprog	English
Emneord	Jordobservationer, billedanalyse
URL	https://www.dmi.dk/publikationer/
ISBN	978-87-7478-756-3
Versionsdato	[4. september 2024
Link til hjemmeside	https://www.dmi.dk/fileadmin/Rapporter/2024/DMI_rapport_24_13.pdf
Copyright	DMI og DTU



Resumé

Dette bachelorprojekt har til formål at undersøge hvordan spredning af lys fra partikler i atmosfæren påvirker billeder af månen, ved sammenligning af halo profiler fra billeder taget fra jorden og fra Den Internationale Rumstation ISS. Vores primære fokus var at analysere månebillederne taget af den danske ESA-astronaut Andreas Mogensen fra Earthshine eksperimentet.

Billederne blev først sorteret og derefter kombineret til et gennemsnitsbillede ved alignment for at reducere støj. Herefter blev pixelintensiteten af haloen målt og de tilhørende lineære fits sammenlignet ved brug af Z-test. ISS-billederne taget af Andreas Mogensen havde en stejlere negativ hældning og større kontrast på tværs af farvebånd sammenlignet med billeder taget fra jorden af fotografen Jens Jacobsen, resultatet indikerer en reduktion af atmosfærisk spredning. Eksperimentet var dog begrænset af optiske artefakter skabt af Cupola modulets vinduer, hvilket havde betydning for mængden af brugbare billeder. Videre analyse ville inkludere forbedring af forsøgsopstillingen og analyse teknikker til at minimere reflekser. Denne rapport fremhæver rum-baseret observationers potentiale til at forbedre jordskins metoden til fremtidig klimaforskning.

Analysis of Andreas Mogensen's moon images

Bachelor's Thesis



Analysis of Andreas Mogensen's moon images

Bachelor's Thesis
2th of June, 2024

By
Mathilde Saltoft Schou

Copyright: Reproduction of this publication in whole or in part must include the customary bibliographic citation, including author attribution, report title, etc.

Cover photo: Andreas Mogensen

Published by: DTU, Department of Space Research and Technology, Elektrovej, building 327, 2800 Kgs. Lyngby Denmark
<https://www.space.dtu.dk/english/>

Approval

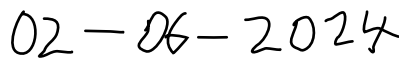
This thesis has been prepared over six months at the Department of Space Research and Technology, at the Technical University of Denmark, DTU, in collaboration with the Danish Meteorological Institute (DMI) in partial fulfilment for the degree Bachelors of Science in Engineering, BSc Eng.

The bachelor's thesis has been carried out under the direct supervision of Mai Winstrup and Peter Thejll. I would like to express my gratitude to Mai Winstrup and Peter Thejll for the guidance and assistance during this process.

Mathilde Saltoft Schou - s214520

A handwritten signature in black ink, appearing to read 'Mathilde', written over a horizontal dotted line.

Signature

A handwritten date '02-06-2024' in black ink, written over a horizontal dotted line.

Date

Abstract

This thesis investigates the impact of atmospheric scattering on images of the Moon by comparing halo profiles from images taken on Earth and from the International Space Station (ISS). Our primary focus was on analyzing the images taken by Danish ESA astronaut Andreas Mogensen as part of the Earthshine experiment. We processed the images by rejecting invalid ones and aligning valid ones to create noise-reduced averages. Pixel intensities were extracted from the halo and compared the linear fits using Z-tests. ISS images, captured by Andreas Mogensen, exhibited larger negative slopes and greater contrast compared to Earth-based images by Jens Jacobsen, indicating reduced atmospheric scattering. Limitations included optical distortions from the ISS cupola windows, reducing usable data. Future research should focus on enhancing observation and image processing techniques to minimize distortions and improve halo profile comparisons. This study highlights the potential of space-based observations to refine Earthshine measurements for climate research.

Contents

Preface	ii
Abstract	iii
1 Introduction	1
2 Background	3
2.1 The Earthshine Experiment	3
2.2 Earth's Albedo And Climate System	3
2.2.1 Albedo	3
2.2.2 Earth's Heat Engine	3
2.2.3 Energy Budget	4
2.3 Albedo Measurement	4
2.3.1 Satellite Methods	5
2.3.2 The Earthshine Method	5
2.4 Limitations of the Earthshine method	5
2.4.1 Mie Scattering	5
2.4.2 Aperature Diffraction	6
3 Data	7
3.1 Method of measurement	7
3.1.1 The sensor	7
3.1.2 The camera	7
3.2 Defects and quality of image data	7
3.3 Data used in this project	8
4 Method	9
4.1 Data Reduction	9
4.1.1 Checking corner values to remove unwanted objects	9
4.1.2 Checking the percentage of overexposed pixels	10
4.2 Color-band Images	13
4.3 Data Preparation - Alignment And Image averaging	14
4.3.1 Spatial Alignment Using Registration And Transformations	14
4.3.2 Rotation	14
4.3.3 Translation	15
4.3.4 Averaging Aligned Images	15
4.4 Data analysis	15
4.4.1 Extracting The Halo Profile	16
4.4.2 Estimate Linear Fits	17
5 Results	19
5.1 Data reduction	19
5.1.1 Data reduction results	22
5.2 Data Preparation - Alignment	22
5.2.1 Alignment Of The ISS Images	22
5.3 Halo Profiles	24
5.3.1 GMT256 Halo Profile	26
5.3.2 JJ16 Halo Profile	26

5.3.3	JJ15 Halo Profiles	27
5.3.4	Linear Fit Comparison	29
6	Discussion	31
6.1	Methods - Data Reduction	31
6.2	Method - Alignment And Averaging	31
6.3	ISS images - Ghost Images	32
6.4	Halo Profile Analysis	32
7	Future Work	35
8	Conclusion	37
	Bibliography	39
A	Energy budget	41
A.1	Energy budget and balance	41
A.2	Surface and atmosphere energy budget	41
B	Results - All halo profiles	43
B.1	Data and standard deviation	43
B.1.1	OLS linear fit of GMT256	48

1 Introduction

The Earthshine experiment is a part of the Danish astronaut Andreas Mogensen's Huginn mission and is a collaboration with the Danish Meteorological Institute (DMI) and the Department of Space from the Danish Technical University (DTU Space). The Earthshine experiment aims to investigate to what extent the scattering of light produced by the atmosphere can be reduced when observing the Moon from outside the atmosphere.

During his time on the International Space Station (ISS), Andreas Mogensen was asked to photograph the Moon close to the New Moon phase through the windows of Cupola. These images collected one month apart, resulted in more than 4500 images. As a part of the experiment, DMI and ESA invited the public to participate by taking pictures of the Moon [1]. The purpose of the experiment is to improve observation methods in climate research by providing more accurate measurements for observations of Earth's albedo, which is essential for understanding Earth's climate. Albedo measurements are greatly affected by Mie scattering caused by the atmosphere, which lowers important contrasts used to estimate the albedo.

This thesis aims to obtain and analyze intensity profiles of light around the Moon - *the halo*, in images taken from ISS and compare them to images photographed from Earth.

The primary objective is to separate the effects of scattering produced by the atmosphere. By analyzing the differences or similarities in the halo profiles, we seek to determine whether the amount of scattered light is significantly lower when observed from space. The goal is to provide valuable insights into the technique for future improvement in climate research

This thesis is structured as follows: In chapter 2 we introduce the background, in chapter 4 we explain the developed methods for the analysis, and in chapter 5 and chapter 6 we show results and discuss these.

2 Background

2.1 The Earthshine Experiment

The purpose of the Earthshine experiment is to investigate to what extent the scattering of light is reduced by observing outside the atmosphere, the to improve methods in climate research. During his time at the international space station, the Danish ESA astronaut Andreas Mogensen photographed the Moon close to the new Moon phase at Moon-rise through the windows of the Cupola module as a part of the Huginn mission [1]. The images were collected 1 month apart and we received over 4500 images. To avoid over-exposure of the images, Andreas tried different camera settings, such as changing the exposure time or ISO number.

As a part of the experiment, DMI and ESA invited the public to participate by taking pictures of the Moon on specific dates providing data for the analysis. From Earth, we received over 1500 images from people across the globe [2].

2.2 Earth's Albedo And Climate System

The incoming solar radiation is the driving force of Earth's climate circulation and the primary energy source. A fraction of the incoming light is reflected into space by clouds, ice and the surface, the amount of reflection determines how much energy enters Earth's climate system. The ratio of incoming light to reflected light is called the albedo.

2.2.1 Albedo

The planetary albedo is defined as the ratio of reflected power. Earth's albedo is the combined effect of both surface and atmosphere. The planetary albedo A_p is expressed as:

$$A_p = \frac{L_{refl}}{L_p} \quad (2.1)$$

Where L_{refl} is the luminosity of the total reflected light, and L_p is the total power intercepted by the planet [3].

2.2.2 Earth's Heat Engine

The incoming solar radiation enters Earth's system and is absorbed, depending on the planetary albedo by the surface and atmosphere and then re-radiated as thermal energy (Infrared - IR) into space. A balance is established between the incoming and outgoing energy flux, preventing the planet from heating up or cooling off. The intensity of incoming solar radiation, known as solar irradiance, varies due to stellar activity and the long-term evolution of the Sun, though these changes are significant only over large timescales. Additionally, solar irradiance is influenced by Earth's orbital factors, including distance from the Sun, orbital eccentricity, and axial tilt. These factors cause seasonal variations and affect Earth's albedo and rotation rate.

The total solar irradiance is the maximum power delivered by the Sun at a surface perpendicular to the path of radiation at TOA. Considering areas close to the Equator at midday the path is almost perpendicular. Increasing latitudes experience a decrease in average solar irradiance as the area receives less radiation because of Earth's spherical shape. Imbalances in solar heating in different regions result in energy transport and circulation through the coupling between the atmosphere and the ocean. The redistribution known as Earth's heat engine works to even out the imbalance through different processes of convection, evaporation, rainfall, winds and circulation of the ocean. It also includes the

transport of heat from the surface and lower atmosphere to space. The net energy flow in and out of the system is noted as Earth's energy budget [3].

2.2.3 Energy Budget

The global mean effective temperature T_{eff} at which it radiates, is determined by the net flow of energy. For the temperature to be stable over long periods the energy budget at the top of the atmosphere must be in balance.

The incoming radiation at the top of the atmosphere - TOA is approximately $1370 [W/m^2]$ noted as S . This is the average amount of total incoming energy times the cross-sectional surface πR_e^2 projected onto the sky and the albedo.

$$E_{in} = (1 - A_p)S\pi R_e^2 \quad (2.2)$$

Where R_e is the radius of the Earth and A_p is the planetary albedo described in subsection 2.2.1. Some of the incoming flux is reflected by the atmosphere, whereas the rest is absorbed - approximately 70% [3].

For simplicity, the Earth is treated as a black body and the absorbed energy is re-emitted as thermal energy following Stephan-Boltzmann law. The incoming heat flux must be equal to the outgoing heat loss to balance the system yielding:

$$E_{out} = 4\pi R_e^2 \sigma T_{eff}^4 \quad (2.3)$$

The outward flux is assumed uniformly emitted across the whole surface area. σ is the Stephan-Boltzmann constant and T_{eff} is the effective temperature. The effective temperature is defined as the theoretical temperature of a black body, required to keep the system in balance. Assuming energy balance, the terms of incoming (2.2) and outgoing energy (2.3) yields.

$$E_{in} = E_{out} \Leftrightarrow T_{eff} = \left(\frac{S}{4\sigma} (1 - A_p) \right)^{1/4} \quad (2.4)$$

Where (2.4) expresses the effective temperature of Earth T_{eff} in terms of the solar constant S , σ being the Stephan-Boltzmann constant and the planetary albedo A_p . This is a simplified expression of the system, a more realistic expression regarding Earth's energy budget must account for the atmosphere and greenhouse effect, as they contribute to the system's temperature see Appendix A. In addition, the presence of an atmosphere also affects the planetary albedo.

2.3 Albedo Measurement

The planetary albedo is an important factor regarding Earth's climate system as shown in 2.2.3 where the temperature of the system depends on the reflectivity of Earth, see (2.4). The planetary albedo determines the amount of energy that enters the system and even small changes affect the mean temperature of Earth. Further, the albedo varies with the reflectivity of Earth's surface, ice, snow and cloud coverage.

A recent publication of a study of Earth's reflectance over the past 20 years has revealed a decline in the global albedo [4]. According to the study of two distinct observation methods, both satellite-based measurements (CERES) and the Earthshine method found agreement on a decline over the past two decades (1998 - 2017). The measured decline in global reflectivity at 1% corresponds to a $\Delta T_{eff} = 0.3K$ global effective temperature increase Equation 2.4.

By acknowledging the significant contribution of A_p climate models should account for change and variation in the albedo according to its dependency on feedback mechanisms changing both atmosphere and surface. Long-term monitoring of the global albedo provides important insights into the climate system and how it's affected by changes in cloud coverage, atmospheric composition and the surface.

2.3.1 Satellite Methods

Satellite measurements of the-top-the-atmosphere (TOA) shortwave radiation, make it possible to derive the albedo, by measuring the TOA shortwave radiation for particular spot [5]. The downside of using satellite measurements, is the lack of global monitoring, needing combined measurements from separate data to reach global resolution. Another major disadvantage is the unknown change in sensitivity of the instruments when exposed to space for long periods.

2.3.2 The Earthshine Method

The Earthshine method is based on observing the moon at specific orbital periods to capture the amount of light illuminating the surface. By photographing the moon when it is close to the phase *new moon*, two light sources are present - the Sun and Earth. Since the Sun is positioned behind the Moon when it is *new*, light from Earth illuminates the surface of the Moon and is seen as a faint glow. The bright side of the Moon (BS) is illuminated by the direct Sunlight whereas the dark side of the Moon (DS) is illuminated by reflected light from the day side of Earth. Then, the reflected light from the surface of the Moon is observed from either Earth or space and used to derive the terrestrial albedo:

$$A_p \propto \frac{I_{dark}}{I_{bright}} \quad (2.5)$$

Where A_p is the albedo, I_{dark} is the intensity of the earthshine, and I_{bright} is the intensity of the side illuminated by the Sun (moonshine) [6]. In short, the principle of the earthshine method is to detect the reflected light from Earth - *the earthshine* illuminating the DS and then compare it to the BS.

2.4 Limitations of the Earthshine method

Observations made from Earth are affected by the surrounding atmosphere and the disturbance must be accounted for. Hence the favourable conditions of observing from space outside the atmosphere.

2.4.1 Mie Scattering

Mie scattering is the scattering of light that occurs when particles are similar or larger than the wavelength of the incident light. Mie scattering, results in scattering of all wavelengths of visible light in all directions resulting in a white appearance or glare around light sources, producing a strong forward scattering peak. Mie scattering is caused by aerosols like dust or water droplets in the atmosphere and depends on the wavelength-to-particle size ratio [7].

The consequence of Mie scattering is the interaction between incoming visible light and water droplets in the atmosphere, which creates a halo around light sources such as the Sun or Moon. This scattered light from the bright side is projected onto the dark side, interfering with Earthshine measurements. As a result, the overall brightness of the background increases, making the faint dark side harder to detect and decreasing the contrast. Additionally, variability in aerosol concentrations causes uneven illumination and background noise. Dust, scratches and imperfections on optics also contribute to scattering disturbances.

Mie scattering and overall atmospheric disturbance are minimized when observing from high altitudes and under favourable weather conditions. Furthermore, image processing techniques, such as accurate background subtraction and calibration, can reduce the effects of scattering. Rayleigh scattering and atmospheric extinction also contribute to increased sky levels.

2.4.2 Aperature Diffraction

Another error contribution originates from the optics, where aperture diffraction confines the optical resolution. Diffraction occurs when light passes through an opening, bending the path of the light and causing interference, resulting in a diffraction pattern.

For optics involving cameras, we consider the case of a circular aperture. In [7], the irradiance of a circular aperture is expressed as

$$I = I_0 \left(\frac{2J_1(\gamma)}{\gamma} \right)^2 \quad (2.6)$$

Where $J_1(\gamma)$ is the first order Bessel function, the irradiance I tends to I_0 when $\gamma \rightarrow 0$, furthermore, the normalized irradiance I/I_0 is at maximum at the center, and the circular aperture yields rotational symmetry about the optical axis[7]. The central spot (the maximum) is called an Airy disc and is the diffracted image, surrounded by concentric rings decreasing in intensity with distance. The angular radius of the Airy disc is $\theta \approx 1.22\lambda/D$ for a circular aperture, depicting the wavelength dependence. The above expression applies to monochromatic light from a point source.

To summarise, Earthshine observations are affected by optics causing diffraction and atmospheric Mie scattering, thus the effect is a combination of the diffraction pattern and the amount of scattering. The purpose is to separate the effects of removing the atmosphere when observing the intensity profile. In this case, we are considering broad-band light and an extended source. The extended object is treated as an adjacent point source and the envelope of the white light intensity follows that of Equation 2.6, the intensity decreases with increasing distance to the maximum following a power function.

3 Data

3.1 Method of measurement

The amount of light on the Moon's surface and its surrounding halo is measured using cameras to capture the intensity in the images. The main components of such cameras are the lens, the sensor and the memory card.

3.1.1 The sensor

Light let into the camera by the lens is detected by a sensor and then processed by the camera. The sensor consists of photodiode arrays which are semiconductors and the most common are the Charge Coupled Device (CCD) or Complementary metal–oxide–semiconductor (CMOS) - both are junction photodiodes. Each pixel measures detected photons and then converts that into a voltage which can be stored as a digital number by the camera [8]. Also, the sensor is sensitive to colours to capture intensity and colour expression.

CMOS sensors, consist of individually addressable photodiodes enabling storage of all pixels at once. Each pixel has individual amplifiers and conversions between photons to charge and charge to voltage. Detection of colour is possible through Color Filter Arrays - referred to as CFA.

The sensor comprises unit cells of 2x2 pixels that detect colour impressions. Band-pass transmission filters for Red, Blue and Green wavelength ranges are coated directly onto the array making each pixel sensitive to a specific color. Considering the choice of CFA, the most commonly used is known as the Bayer pattern, where each unit cell involves one red, one blue and two green pixels. Subsequently, two green band-pass filters per unit cell result in a better gain of colour impression as the eye is more sensitive towards the green light. Detected light across the sensor is filtered and then demosaicing is performed upon the CFA to reconstruct color information by interpolation. The resulting colour image is saved along with the raw image file.

3.1.2 The camera

The sensor is the light-capturing element of a digital camera converting photons to voltage. All cells are emptied to remove additional charges before capturing an image [8]. Digital cameras use the shutter to control the amount of light that enters the sensor. By opening the shutter to capture an image and closing it again to stop the measurement of light. The time at which the shutter is open is the exposure time. The longer the exposure time the more incident light is permitted to enter the camera and most importantly - the sensor, larger amounts of light yield higher voltages. If the exposure time is too high the image becomes overexposed, as too much incident light saturates the electronics. On the contrary, low exposure time results in underexposure and loss of linearity.

Large amounts of data within the image are lost if the pixels are overexposed and therefore values are fixed at the maximum value. This results from over-saturation of the sensor and the intensity histogram is shifted towards the brighter side of the spectrum. Leading to a loss of linearity and contrast as values out of range are clipped according to the data type. Other types of missing data per pixel arise from so-called dead, stuck or hot pixels.

3.2 Defects and quality of image data

Dead pixels are the direct effect of missing power supply to the specific pixel. The sensor receives no power resulting in dead pixels to be fixed at the same value. Dead pixels are

permanently damaged and are therefore always in the same spot. The cause is often burnt pixels caused by radiation striking the semiconductors that make up the sensor.

Stuck pixels are in the same way as dead pixels stuck at a specific value. Stuck pixels are fixed at the maximum possible value and the photodiodes always receive power, unlike dead pixels.

Hot pixels are defects caused by high energy cosmic rays, resulting in pixels giving off large signals compared to the neighbouring pixels [9]. Hot pixels also appear more frequently as the temperature increases. Regarding digital cameras, the sensor becomes more receptive towards heating at high ISO settings. Hot pixels are visible as high values in pixel intensity. The increase in signal is due to a leak of electrical charge into the sensor. As the sensor is a photodiode dark current noise applies. The dark current is a constant background contribution and is defined as the signal level when the photodiode is not illuminated. So-called "dark frames" correct added noise by exposure with a closed shutter before or after the light exposure [10].

Cosmic rays, also affect the image signal by damaging the sensor or causing temporary distortion. Cosmic rays are sub-atomic high energy particles moving through space at velocities close to the speed of light [11].

3.3 Data used in this project

This project analyzes images of the Moon from the climate experiment *Earthshine*, which includes photographs taken by Danish ESA astronaut Andreas Mogensen as part of the Huginn mission. Photographers from around the world contributed their images of the Moon. The images used in this project are RAW files. Cameras store images as RAW files, accompanied by an EXIF (Exchangeable Image File) header and a compressed image format such as JPEG (Joint Photographic Experts Group). The EXIF header stores specific settings and information about the image and camera as metadata tags.

Table 3.1, shows the data used in the analysis.

Metadata for each dataset							
Directory	Date	Age of the Moon	Camera	Data type (BPS)	File type	Image width	Image height
GMT009	2024:01:09	27.2 days, 6.1%	NIKON D5 Ver.N.10	12	NEF	5584	3728
GMT039	2024:02:08	27.7 days, 3.8%	NIKON D5 Ver.N.10	12	NEF	5584	3728
GMT256	2023:11:10	26.6 days, 9.1%	NIKON D5 Ver.N.10	12	NEF	5584	3728
JJ-15	2023:11:15	2.2 days, 5.4%	Canon EOS 80D	14	CR2	6288	4056
JJ-16	2023:11:16	3.2 days, 11.7%	Canon EOS 80D	14	CR2	6288	4056

Table 3.1: Table displaying metadata and information about the different data used in the analysis.

The images by Jens Jacobsen were taken on La Palma, a part of the Canary Islands at a high altitude providing favourable conditions for observations. He used a telescope lens mounted on a Canon camera. The image data from Jens Jacobsen is labeled JJ15 and JJ16.

The images from Andreas Mogensen comprise the datasets GMT009, GMT039, and GMT256. These images were captured near Moonrise through the Cupola module windows using a Nikon D5 camera with a 400mm lens. Notably, the GMT256 images were taken with a different Nikon D5 camera than those used for GMT009 and GMT039. The cameras, having been onboard the ISS for an extended period, may exhibit defects due to exposure to cosmic rays. The Cupola windows introduced reflected images of the Moon, known as *ghost images*, into the images. Andreas Mogensen's image files are identified by filenames starting with *iss070e*.

4 Method

This section describes the necessary methods used to analyze the image data. The main steps are data reduction, data preparation and data analysis. First, we must remove inappropriate data by data reduction. Then prepare the data for analysis by combining individual images into one average image for the individual color-bands of each dataset to reduce noise. The last step is to extract the pixel intensities of the resulting images' halo, then compare each profile's linear fits and analyze differences between the different image data.

4.1 Data Reduction

We have received a large amount of data from the ISS and Earth, the data must be filtered so images containing unwanted features are rejected before further analysis. Before we initiate data reduction we visually inspect the ISS images from different days to get a visual estimate of the quality. While comparing the images we found unwanted features and defects such as dead pixels, cosmic rays, objects other than the moon, light in the background and overexposed images. Such images must be rejected. We then implement an automatic filter to sort the data based on the above-mentioned.

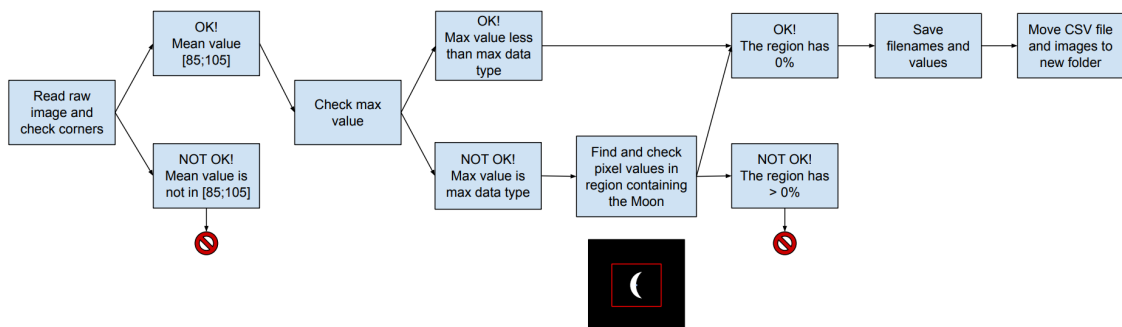


Figure 4.1: RAW image filter overview for the ISS images.

The filter validates the images based on two steps, by checking the mean value of the background for each corner and then examining the pixel values.

4.1.1 Checking corner values to remove unwanted objects

From the initial inspection of the received data from the ISS, we see structural elements from the space station in some of the images. In addition, images containing gradients around the borders originating from light sources other than the moon have been spotted among the data. Such images must be rejected. We implement a filter capable of finding and removing invalid images as defined above.

First and foremost, each RAW image file is loaded and the sensor array data is extracted to create an image matrix, where each cell represents a pixel. Secondly, a box with a dimension of 500x500 pixels is placed inside each corner and then the mean value of the region is extracted resulting in 4 corner values in total. The expected background value is $\mu_{sky} = 100 \pm 1$ of the Nikon D5 images.

If the image contains any objects other than the moon or other light sources are present we expect mean corner values $\neq \mu_{sky}$. The corner filter calculates the mean value and checks if any of the four is out of range [85; 105] and removes the invalid ones.

Figure 5.2 shows the found values inside each of the four corners of a raw image with each area marked by a box.

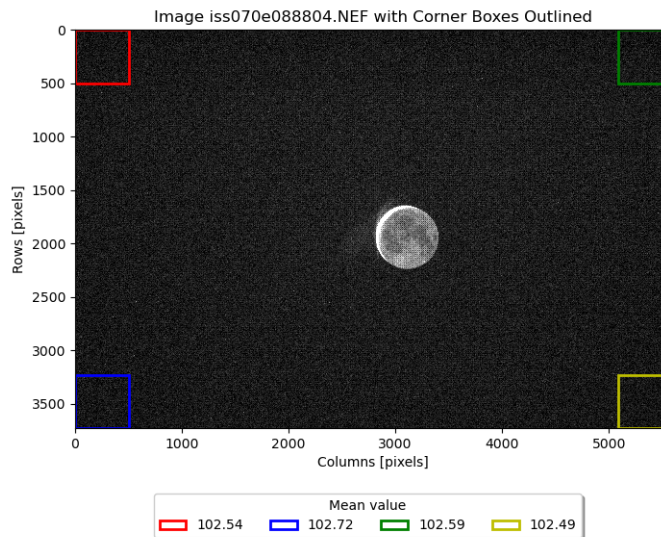


Figure 4.2: Corner values of iss070e088804.NEF showed in the range of 5th and 98.89th percentiles. The filter found no invalid values as all are within the defined range [85; 105].

In contrast, Figure 4.3 illustrates the example of an invalid image, the values inside the top left and right boxes exceed the limit of 105 and are therefore removed.

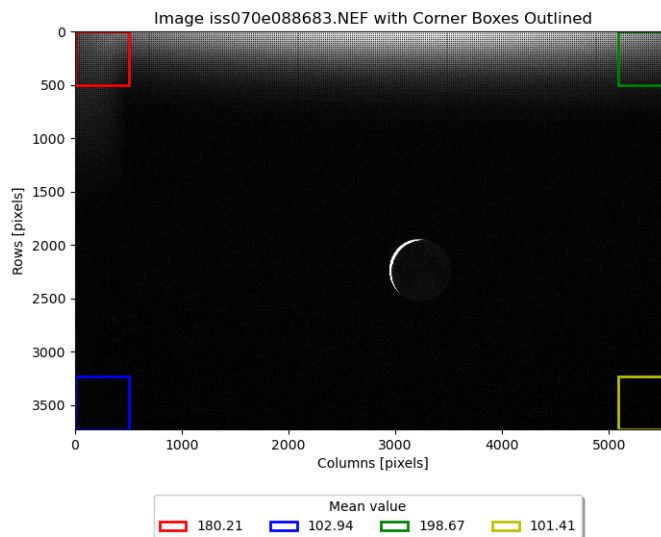


Figure 4.3: Corner values of iss070e088683.NEF showed in the range of 5th and 98.89th percentiles. The values inside the top left and right boxes exceed the limits.

4.1.2 Checking the percentage of overexposed pixels

The next step is to investigate the pixel intensities inside the images, as we can not use over-exposed images. The maximum pixel value is found for each raw image containing

the whole pixel array and therefore all colour channels. The purpose of the procedure is to check if the image contains possible overexposed pixels which is undesirable. Overexposed images lack linearity and thus images are disqualified for further analysis, as mentioned in section 3.2.

The filter saves data, that could have been removed if we allowed no pixels equal to the maximum possible value, this increases the the signal-to-noise ratio when later stacking the images.

The camera type must be accounted for when applying this method as the maximum value varies according to the data type. Since Andreas Mogensen is using a Nikon D5 camera onboard the ISS the maximum possible pixel value is determined by the data type. The Nikon D5 camera stores the image in the data type unit12 which ranges from [0; 4095] enabling high contrast and detailed image data. Therefore, when checking for overexposed images in the case of Andreas Mogensen's images, the max possible pixel value is 4095¹.

All raw images are processed and investigated such that overexposed images must be removed. The region containing the moon (the region of interest - ROI) is analysed to avoid false classification and optimise the data amount. We have encountered images with less than 3 pixels where the values were at their max caused by cosmic rays or damaged areas on the sensor, see section 3.2.

Invalid Pixel Filter

We now check if the image data contains overexposed or defects in the region we wish to analyse. Each image is inspected using well-known digital image processing methods, in this case, mathematical morphology, image moments and segmentation [8].

The region of interest is found by applying the steps below when processing the image:

1. Background subtraction
2. Create binary image
3. Morphology Operation - Erosion
4. Clear border
5. Find the centroid of the binary image
6. Create a bounding box
7. Extract region of interest - ROI
8. Image statistics of pixels inside ROI
9. Remove invalid image files

The first part is to optimize the segmentation of the image by dividing the image into two parts - foreground and background. The segmentation is based upon the assumption of pronounced differences in pixel intensity between the moon (the bright side) and the background (the sky). Each raw image is read and no interpolation or de-mosaic is applied to preserve the raw information within the image from now on noted as $f(x, y)$. yielding an array of grey scale values as no colour interpretation is performed.

¹The range for the datatype unsigned integer 12-bit format is $[0 \ 2^{12} - 1]$

Background Subtraction

After removing invalid images according to corner values, we assume a negligible change in background values across all image data. The four corner values are extracted from the data frame and then used to determine the best value representing the background. We select the smallest value among the four as the mean background value μ_{sky} to preserve as much information as possible.

$$g(x, y) = f(x, y) - \mu_{sky} \quad (4.1)$$

$g(x, y)$ is the resulting background subtracted image.

Create Binary Image

We aim at extracting the Moon, to investigate the properties of the region containing the Moon. The image $g(x, y)$ from Equation 4.1 is segmented into foreground and background to create a binary image by applying the point processing operation *thresholding* $g(x, y)$. The threshold is set to the value $T = 10$ and applied in the following way:

$$\text{Binary image} = B(x, y) = \begin{cases} 1 & g(x, y) > T \\ 0 & \text{otherwise} \end{cases}, \quad \text{for } T = 10 \quad (4.2)$$

A binary image has two values: 0 = black and 1 = white. Where values equal to 0 represent the background and 1 is the foreground. All pixels in the background subtracted image that have values above the threshold are set to 1 as these satisfy the condition.

Erosion

The Moon is expected to be the largest object within the binary image. We aim to extract the Moon as the primary BLOB - Binary Large Object, by removing the remaining noise from the global operation thresholding. BLOBs are groups of pixels defined by each pixel's connectivity to its surrounding neighbours.

The morphological operation erosion removes the smaller BLOBs and noise using a structuring element similar to a kernel in neighbourhood processing. A hit-or-fit method applies the structuring element to each pixel. Erosion uses the method fit, where the structuring element is placed at the position of each pixel and evaluates the pixel value in the same position as the structuring element. If the pixel fits the structuring element, the value is set to 1 and otherwise 0. The operation is defined as:

$$B_e(x, y) = B(x, y) \ominus SE \quad (4.3)$$

$B_e(x, y)$ is the resulting image and SE is the structuring element of the type disc and size 1. A disc-shaped structuring element results in round edges, SE is illustrated below:

$$SE = \begin{bmatrix} 0 & 1 & 0 \\ 1 & 1 & 1 \\ 0 & 1 & 0 \end{bmatrix}$$

The resulting image is cleared from noise by this erosion. Secondly, larger BLOBs connected to the image border are removed. The binary image is now ready for further analysis.

The Centroid

To extract the region of interest, we implement a method for finding the Moon using BLOB analysis. The aim is to extract and classify the objects present after segmentation. Pixels with values equal to 1 are extracted and labelled as foreground pixels. Then BLOB classification is applied to the labelled BLOBs to extract the binary image's Centroid². The Centroid is calculated as the weighted sum of all points in the BLOB. The centroid is defined as:

$$x_c = \frac{1}{N} \sum_{i=1}^N x_i \wedge y_c = \frac{1}{N} \sum_{i=1}^N y_i \quad (4.4)$$

N is the number of pixels inside the BLOB. We derive the centroid coordinates based on all BLOBs present [8].

Bounding Box And ROI

The derived Centroid coordinates (x_c, y_c) are then used to create a bounding box with the centre equal to that of the Centroid. We define a rectangular box with the height $h = 1300$ and the width $w = 1500$ measured in [pixels]. The dimensions of the bounding box containing the Region Of Interest (ROI) are given by:

$$W_{BB} = x_{max} - x_{min} = (x_c + w/2) - (x_c - w/2) \quad (4.5)$$

$$H_{BB} = y_{max} - y_{min} = (y_c + h/2) - (y_c - h/2) \quad (4.6)$$

W_{BB} is the width of the bounding box and H_{BB} is the height as integers. The area of the bounding box is applied to the original raw image to extract the ROI. If the bounding box exceeds the image's border, the image is flagged as invalid since the halo is out of range.

Image statistics inside ROI

The last step is to calculate the number of max value pixels N_{ROI} inside the cutout to conclude if the image is over-exposed:

$$P_{max} = \frac{N_{ROI}}{N_{max}} \cdot 100\% \quad (4.7)$$

If the percentage $P_{max} > 0\%$ the image is flagged as invalid and will be removed from the data.

Images from Earth are filtered, following the same approach described in Figure 4.1 with minor adjustments and removal of the corner filter. The range is redefined to [0; 16383] since the data is in the 14-bit uint format³.

4.2 Color-band Images

The next part of data preparation is to sort and group the sorted images according to the CFA as mentioned in subsection 3.1.1. As we recall, the raw images comprise unit cells sensitive to specific color-bands.

To split each image into its color components R, G, G2 and B, all pixels must be extracted according to the Bayer pattern. The desired result is obtained using 4 channels from the LibRaw library (raw image decoder) [14]. LibRaw 4channels can decode the underlying CFA from the metadata and then create 4 new images for each colour saved as uint16 tiff format.

²The centroid is also noted as "center of mass" or central gravity

³The script uses functions from scikit-image [12] and rawpy [13].

The two green color-bands G and G2 are kept as separate images, making it possible to estimate an error within the image data, as we would expect them to have equal values as they are sensitive towards the same wavelengths, large differences indicate errors.

4.3 Data Preparation - Alignment And Image averaging

A crucial step is to combine the images in each color-band to reduce noise and optimise the analysis. We create one average image for each color-band: R, G, G2 and B. All images must be spatially aligned (registered) to avoid blurring when creating the average image. Therefore, we also implement a method for aligning the images, before the addition. Comparisons between images are obtained using image subtraction to derive differences, known as a similarity measure [8].

All images are converted from the datatype unsigned integer (unit) into float64, to avoid interpolation and errors from processing software when converting back and forth between data types. Keeping the data as float64 type avoids over- and underflow as the unsigned integer format is restricted to positive integers.

4.3.1 Spatial Alignment Using Registration And Transformations

To reduce noise by image averaging, the images must be aligned, to produce the best combined image of the Moon as mentioned in section 4.3. We expect rotation and translation between each image.

According to [8], the transform T is described by a set of parameters yielding the most optimal fit possible with an object function F defined by:

$$F = S(\mathcal{R}, T(\mathcal{T})) \quad (4.8)$$

The transformed template image is noted by $T(\mathcal{T})$ and S is the similarity measure between the two images. We choose cross-correlation as the similarity measuring function for registration similar to template matching. From now on, we note the reference \mathcal{R} as f_R and template image \mathcal{T} as f_T . Cross-correlation is a registration method based on intensity. "Image Registration is an important application of digital image processing to align images" [15].

Assuming scale invariance, rotational and translational shifts are obtained by cross-correlation and applied to the template image as the inverse transform. As the reference image f_R , we select an image with an appropriate object location, where the Moon is positioned close to the centre. All remaining images are defined as transformed versions of f_R , labelled template images f_T . For every f_t within the dataset, the correlation between f_R and f_T is obtained by first comparing the differences in a polar coordinate system, to estimate the angle of rotation. Immediately after applying the inverse transform of the rotation, f_T is once more compared to f_R by extracting the translation using cross-correlation to align the images.

4.3.2 Rotation

Images conducted by Andreas Mogensen differ in the displacement of coordinates by translation and rotation as he was floating. The assumed difference is formulated as: $f_T(x, y) = f_R(x \cos\theta + y \sin\theta - x_0, -x \sin\theta + y \cos\theta - y_0)$ [16].

Both images f_R and f_T are smoothed using a median filter with a disc-shaped structuring element of size 5 before computing the cross-correlation. The rotational shift is derived following the same approach as [17], the method is also robust towards scale differences. The methodology is similar to that of the Fourier-Mellin Transform [18].

Following the method of [17], the smoothed images are band-pass filtered, and then *window* images are obtained by applying the Hanning function. The next step is to create shifted FFT magnitudes, defined as the absolute value of the shifted 2-dimensional FFT of the images. To find the rotation angle and account for potential scaling, we transform the FFT magnitude images using the log-polar transform, then we calculate the cross-correlation of half of the FFTs. The cross-correlation of two images is described in subsection 4.3.3. The recovered angle is then expressed in *[deg]* and applied to f_T . In addition, the script iterates over different input variables for the upper limit of the band-pass filter to find the minimal displacement error. After de-rotation, the images only differ in translation and the transform is obtained using the same method as subsection 4.3.3.

4.3.3 Translation

The translation of the template image f_T to the reference f_R is derived by application of the Fourier shift theorem assuming displacement as the only difference $f_T(x, y) = f_R(x - x_0, y - y_0)$ [16].

We derive the frequencies of the smoothed f_R and f_T by using the fast Fourier transform - short *FFT*, a fast algorithm for the discrete Fourier transform sometimes referred to as *DFT*. Applying the N-dimensional *FFT* yields the reference and template image spectrum in the frequency domain:

$$F_R = FFT(f_R) \wedge F_T = FFT(f_T)$$

The Fourier transform of the correlation function is given by the product $F_R \cdot F_T^*$ ⁴. The similarity S is defined as the cross-correlation function as the inverse transform of the product:

$$S = FFT^{-1}(F_R \cdot F_T^*) \quad (4.9)$$

Now, the shift (translation) is equal to the coordinates of the maximum of S see (4.10).

$$(\Delta x, \Delta y) = arg \max(S) \quad (4.10)$$

Finally, the positional shift is applied to f_T by the inverse transform, cropped borders are handled by "wrapping the edges" to avoid missing values[12].

When aligning images from Earth, we only account for translation as we have encountered no rotation between images.

4.3.4 Averaging Aligned Images

Image averaging - sometimes noted as image addition, is an arithmetic operation combining n images of equal size by addition [15]. The operation of addition is expressed by

$$g(x, y) = f_1(x, y) + f_2(x, y) \quad (4.11)$$

In (4.11) $g(x, y)$ is the product of adding the two images f_1 and f_2 of equal size. The purpose is to reduce noise by creating an average image using the sum of n images divided by the amount n , assuming all images are products of the true pixel values with added Gaussian noise. The result is an average image with an increased signal-to-noise ratio, as a factor of \sqrt{n} reduces the noise [8].

4.4 Data analysis

The final part measures the pixel intensity along a line, starting at the border between the bright side of the Moon and the background and terminating far from the Moon. The resulting profiles are normalized to compare the differences in halo intensities between the images from Earth and ISS.

⁴Notation: The symbol [*] notes the complex conjugated.

4.4.1 Extracting The Halo Profile

To extract the halo profiles, we process the images using the same procedure as subsection 4.1.2, to find the starting point for the profile measurement. The aim is to find a point inside the Moon disk near the bright side and close to the centre of the *crescent*. As we already implemented a method of extracting such features in subsection 4.1.2, the function is adjusted and the centroid coordinates are then used as the starting point for our measurements. Pixels within a circular section are defined by a 10-degree angular range, centered approximately outside and perpendicular to the bright side of the Moon. We Measure the pixel intensities along each of the 10 profile lines by interpolation. Figure 4.4, illustrates the drawn profiles within the given angle range for different images.

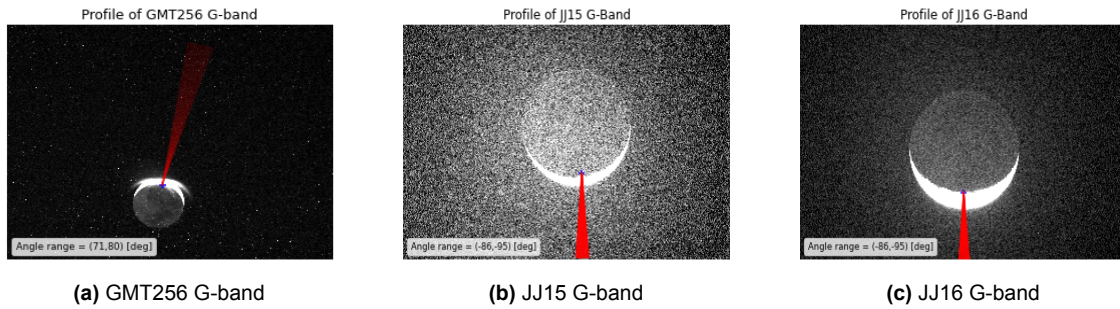


Figure 4.4: The Region of measurements for the images GMT256, JJ15 and JJ16 in the G-band visualized in the 5th to 99.89th percentiles.

The range of angles used for each profile measurement is illustrated in Table 4.1

Angle range					
Dataset	GMT009	GMT039	GMT256	JJ-15	JJ-16
Angle range [deg]	[46; 55]	[136; 145]	[71; 80]	[-86; -95]	[-86; -95]

Table 4.1: The defined angle range for each dataset in [deg].

For each profile intensity measurement at a given angle, the region where the profile passes through the halo is determined during data reduction. Thus, removing parts of the profile that contain pixels from the bright side of the moon, and a new starting point are defined based on the part of the curve where the intensity decreases most rapidly. This point is assumed to be the boundary between the bright side and the sky background.

We identify the steepest negative slope by calculating the numerical derivative of the distances between each measured pixel intensity and the initial point. This allows us to find the part of the profile with the steepest decrease in intensity, defined as the global minimum of the derivative. The section up to this point is removed, the resulting data frame retains only the rows with measured intensities and distances for the region outside the Moon.

The halo profile is normalized in intensity and distance for each given angle. Pixel intensities are expressed as the ratio relative to the first point of the halo intensity I/I_0 . Similarly, the distances are normalized by subtracting the value of the initial distance to the centroid and then dividing all distances by the radius of the Moon, resulting in distances expressed as pixel indices. We found the following radii according to the apparent size of the Moon, the radius in Jens Jacobsen's images $R_{JJ} \approx 496.7$ [pixels] and the radius in Andreas Mogensen's images $R_{ISS} \approx 154.7$ [pixels].

The resulting halo profile is expected to be a power function, as the pixel intensity decreases as the distance to the source increases as described in subsection 2.4.2.

4.4.2 Estimate Linear Fits

Next, all halo profiles for a given image, measured at different angles within the defined range, are combined into a single halo profile. The pixel intensities are averaged for each point, along with the average distance. In addition, the standard deviation of the pixel intensity for each dataset is also calculated as a radial function.

Assuming the normalized pixel intensities will decrease as a function of the distance expressed by a negative power function explained by the behaviour of the PDF, see subsection 2.4.2. We obtain a linear graph by taking the logarithm on both sides of the function Equation 4.12.

$$I(r) = \frac{1}{r^b} \Leftrightarrow \log_{10} I(r) = -b \log_{10} r \quad (4.12)$$

The normalized pixel intensity corresponds to a linear function where the slope is the exponent of the original power function. The pixel intensity of the Normalized profile starts at the value of 1 because of $I_0/I_0 = 1$ and decreases with increasing distance. On each dataset, the section of the profile best representing a linear profile is selected for the linear fit using the *ordinary least square* method [19].

Lastly, we compare the computed slopes for each image using a Z-test Z:

$$Z = \frac{b_1 - b_2}{\sqrt{s_1^2 + s_2^2}} \quad (4.13)$$

Using Equation 4.13, the significance of the difference between slopes b_1 and b_2 , weighted by the standard errors of each slope s_1 and s_2 . Finally, we contrast the slopes of the linear models of the halo profiles for each color-band within an image, and then analyse the different slopes for the same colors in different images. To estimate the significance, we choose a threshold of $Z = 2$ to indicate significance.

We expect the various datasets to be influenced by the same diffraction effects originating from the optics. In contrast, Mie scattering should only occur when observing through an atmosphere, and its contributions are expected to impact the slope of the halo profiles.

5 Results

5.1 Data reduction

This section shows results from the developed software to filter the images according to the criteria defined in subsection 4.1.2 to reject over-exposed images.

The following figures illustrate an example of a potentially overexposed image processed by the filter. The chosen image file "iss070e088804.NEF" is from the GMT0039 dataset and the data type is 12-bit with values ranging from [0, 4095]. The filter found 2893 pixels with values of 4095, the image must undergo further analysis.

Figure 5.1 illustrates the region of iss070e088804.NEF that contains pixel values equal to 4095 marked by a bounding circle. The pixels within the highlighted area correspond to the position of the bright side of the moon. This suggests that the image is likely overexposed, particularly if the number of pixels with maximum intensity values exceeds 100 in the same area.

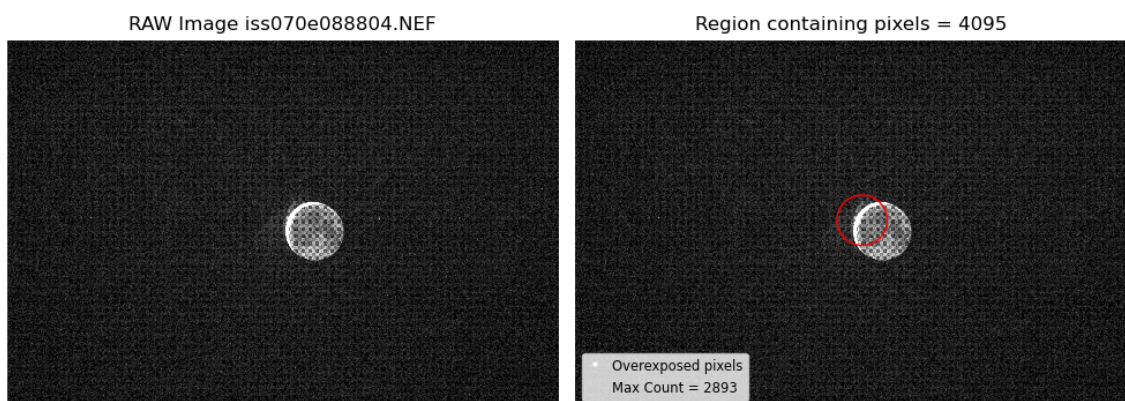


Figure 5.1: Left: RAW image iss070e088804.NEF. Right: RAW image iss070e088804.NEF and bounding circle (red) containing the region of all pixels = 4095 and a legend displaying the count. Both are shown in the range of 5th and 98.89th percentiles

To investigate whether the image is overexposed, a binary image for which we find the centroid and a bounding box, as described in subsection 4.1.2. The filter presumes the moon to be the identified BLOB and, the region of interest (ROI) is delineated as the image content confined within this bounding box illustrated below in figure: 5.2.

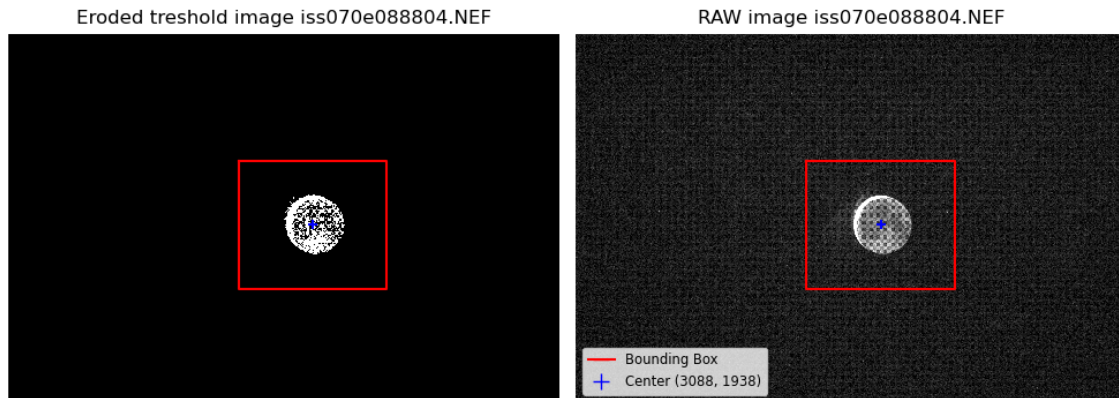
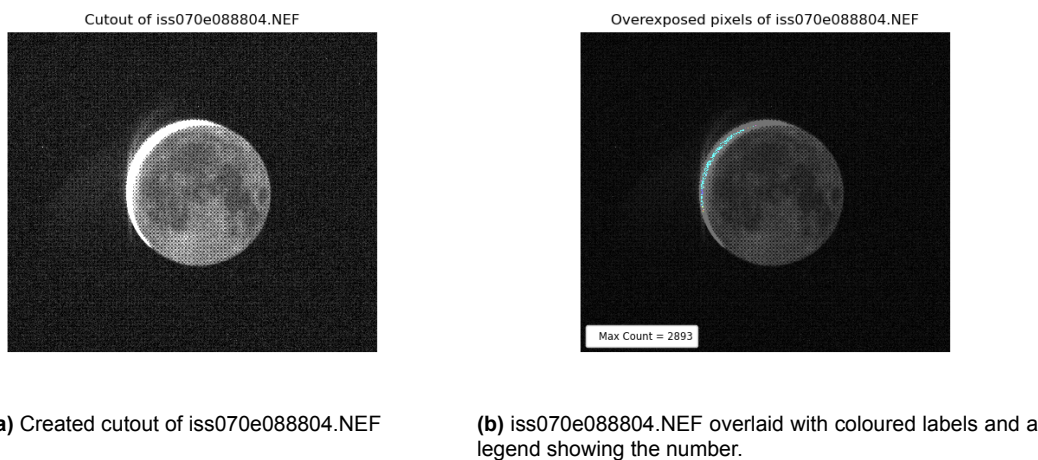


Figure 5.2: Left: The eroded binary image is used as input to calculate the centroid (blue) and the bounding box (red). Right: The original RAW image is shown in the range of 5th and 98.89th percentiles compared to the eroded binary image.

A cutout of the original RAW image is obtained using the bounding box, to reduce the image to the desired content see Figure 5.3a. The new image is limited to the region of interest, enabling appropriate image statistics to validate the quality. The filter checks if the ROI holds any pixels with values at 4095 and counts them. Figure 5.3b illustrates the result, where pixels at 4095 are labelled and coloured, then visually displayed by overlaying the cutout with the found labels.



(a) Created cutout of iss070e088804.NEF

(b) iss070e088804.NEF overlaid with coloured labels and a legend showing the number.

Figure 5.3: Combined Figures a and b. The images are shown in the range of the 5th and 98.89th percentiles.

It is clear, that all pixels with maximum value are situated on the bright side of the Moon. This suggests overexposure within the image, leading to its categorization as invalid and subsequent removal from the dataset.

We now consider the case of image iss070e088646.NEF. The image is processed by checking the values inside the image's corners. The image has passed the first check and the maximum pixel value is found and then processed by the filter. The filter found 3 pixels of the value 4095, and Figure 5.4 shows the output.

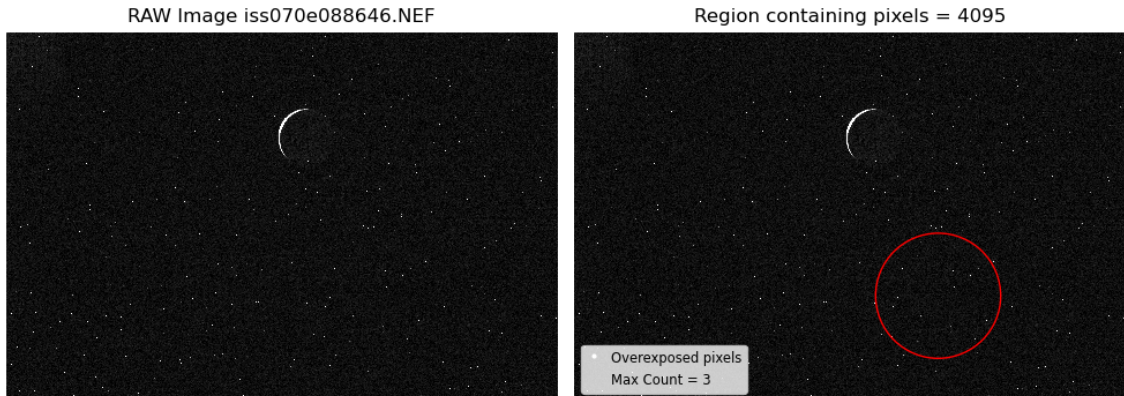


Figure 5.4: Left: RAW image iss070e088646.NEF. Right: RAW image iss070e088646.NEF and bounding circle (red) containing the region of all pixels = 4095 and a legend displaying the count. Both are shown in the range of 5th and 98.89th percentiles

From Figure 5.4, it is clear that the found pixels marked by a red circle, are located in an area below the Moon. The image is investigated further, by finding the ROI and the content following the procedure described in section 5.1. A cutout is created using the centroid as the common centre and the predefined dimensions, and in this region, we investigate whether the defects are included in this area or located outside.

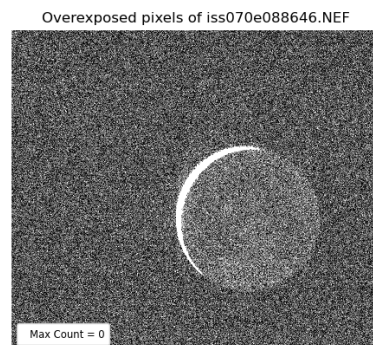


Figure 5.5: Cutout of iss070e088646.NEF showed in the range of the 5th and 98.9th percentiles. The legend shows the number of found pixels.

The filter found no pixels with values 4095 inside the ROI see Figure 5.5. Since no pixels are fixed at the max value, the hypothesis of the image being potentially overexposed is proved wrong. This means the image is deemed valid, and the filter moves to the next image.

5.1.1 Data reduction results

The results demonstrate the efficiency of the filtering process of the analysis, showing the number of images saved by the filter that would have been rejected. The results of the developed method to reject invalid images are presented in Table 5.1:

Result of data reduction					
Directory	GMT009-16-08	GMT039-13-18	GMT256-ESA-1000	JJ-15	JJ-16
Before	520	1070	115	35	98
After	132	251	104	32	47
Saved data	42	70	80	0	0
Accuracy	99.8%	99.3%	100.0%	100.0%	100.0%

Table 5.1: The number of image files before and after using the data reduction filter, the number of saved files (hot pixels) and the accuracy. Note: The accuracy is strictly based on how well the filter was able to detect the defined defect and not other criteria leading to the removal of data afterwards.

5.2 Data Preparation - Alignment

5.2.1 Alignment Of The ISS Images

One of the main challenges was to align all images within a color-band, to create a combined average image increasing the signal-to-noise ratio and optimizing the intended halo profile measurement.

The proposed solution described in subsection 4.3.1 is illustrated in the following figures, using the example of alignment of a template image "iss070e089232" and the chosen reference image "iss070e089512" from GMT039 in the G-band. Before processing the images, they are converted to the data type float64, pixel values are now in the range of [0; 1]. The data type also allows pixel values out of the range when applying different arithmetic operations such as subtraction, which ensures against overflow.

Alignment parameters			
Template image	Angle [deg]	Shift c [pixels]	Shift r [pixels]
iss070e089232	-11.59	206	-254

Table 5.2: The found parameters using cross-correlation between iss070e089232 and iss070e089512, the parameters are the angle, the shift in columns, and the shift in rows. Note the translation is derived after de-rotation.

The script analyzes and applies the found transformation parameters to the template while iterating over variables, finding the best match and yielding minimal differences.

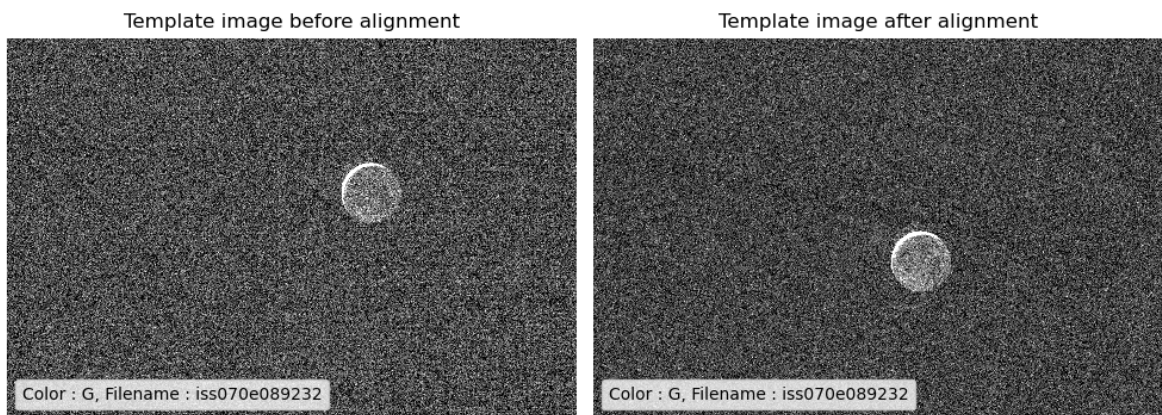


Figure 5.6: The template image before alignment (left) compared to the same image after alignment (right). shown in the range of 5th and 98.89th percentiles

Figure 5.6 illustrate the difference before and after aligning the template image "iss070e089232", see Table 5.2. The image has been rotated and translated to match the reference image, see Figure 5.7 below.

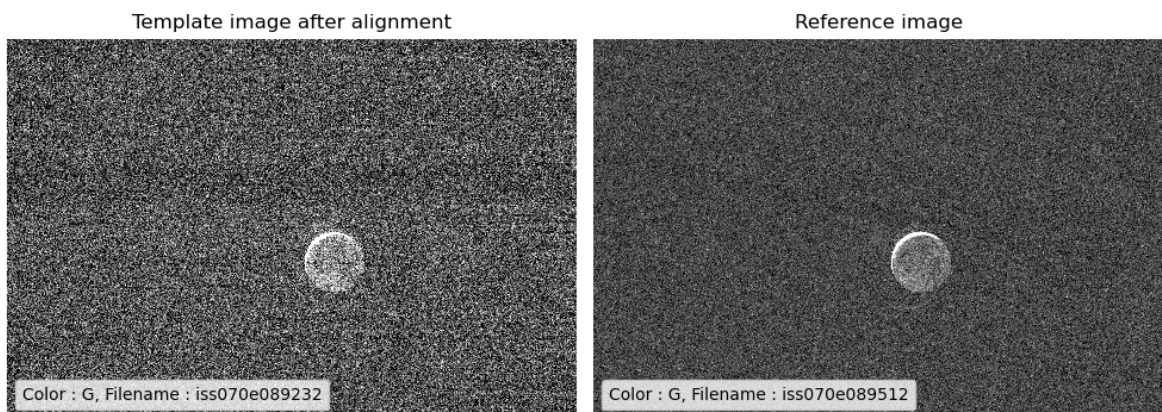
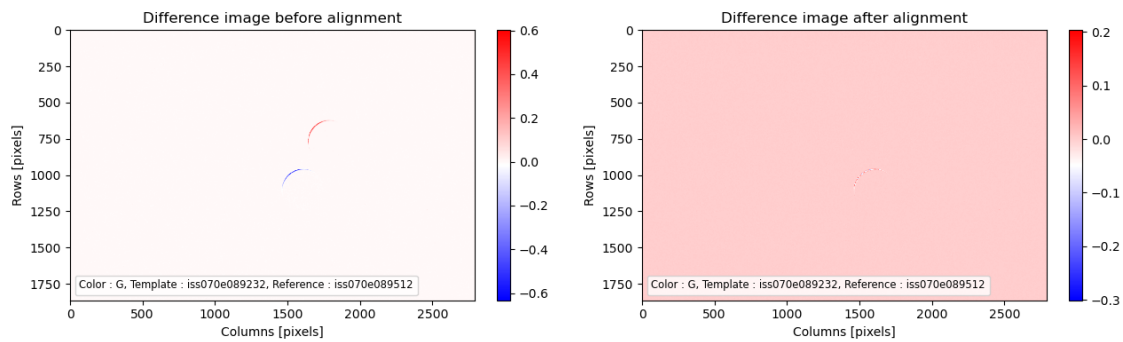


Figure 5.7: The template image after alignment (left) compared to the reference image (right). Both are shown in the range of 5th and 98.89th percentiles

Lastly Figure 5.8 compares the difference image before and after alignment, and the colour bar shows the pixel intensities.



(a) The difference of image before alignment

(b) The difference image after alignment.

Figure 5.8: Figure 5.8a, shows a clear difference between the template image (red) and reference image (blue). Figure 5.8b, shows the clear decrease in differences after alignment. Both color bars show the pixel intensities of the difference image.

From Figure 5.8b, it is clear, that the differences have been significantly reduced from Figure 5.8a. The remaining differences seen in Figure 5.8b could be due to miss alignment or the template image having different exposure.

Images from GMT009 and GMT039 were processed similarly, by choosing an arbitrary reference image located near the center. This was implemented for GMT256, such that all color-bands were aligned using the same reference image, to avoid different orientations for each color of the same RAW image.

Images from Jens Jacobsen are processed and aligned similarly except for de-rotation as we found no rotational differences between each image, again different reference images were used for each color-band within a dataset. This leads to small differences in the object location resulting in small variations in distances from the bright side to the image border.

5.3 Halo Profiles

The resulting halo profiles for the 5 different datasets for each of the four color-bands. In Figure 5.9, a tendency towards a decline in intensity with increasing distance along the profile.

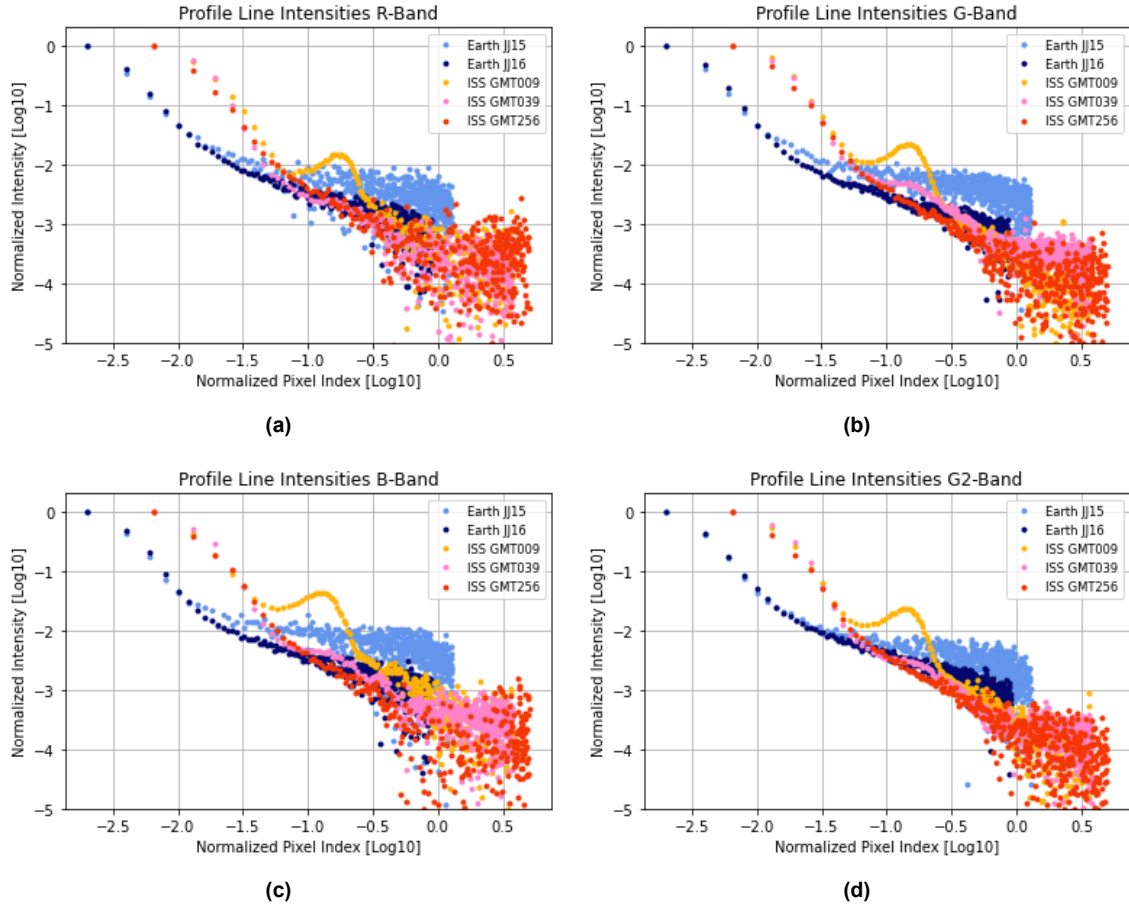


Figure 5.9: Loglog plot of the halo profile intensities for GMT009, GMT039, GMT256, JJ15 and JJ16. The vertical axis is the normalized pixel intensity ranging from $[I_0; 10^{-5} I_0]$, and the horizontal axis is the normalized distance in pixels as a fraction of the apparent radius of the Moon for each image.

The axes of the plot represent the log-transformed (base 10) normalized data for each profile. The vertical axis is the normalized pixel intensities as a function of the normalized distances along the profile, expressed as a pixel index on the horizontal. The normalized pixel index is the distance given in pixels normalized by the apparent size of the radius. The horizontal offset between the data is explained by differences according to the size of the Moon, and simultaneously a limiting factor of the profile length. The moon-to-frame size ratio is smaller for the ISS data, whereas the Moon in the Earth data takes up much more space.

We chose to exclude GMT009 and GMT039 from further analysis because of the present defects. For GMT009 a clear second peak in intensity is seen at a distance of -0.8 due to a strong reflection of the BS, the peak is present in all color-bands. Similar to GMT009, we found regions of increasing and decreasing intensities in the profiles of GMT039 for distances in $[-1.1; -0.3]$.

To avoid errors from inaccurate alignment, measurements at distances less than approximately $0.03R_{JJ}$ and $0.08R_{ISS}$ are excluded when fitting an OLS fit to the data. Furthermore, we also chose to ignore data points at distances larger than $0.63R_{JJ}$ for the JJ-images and $1.26R_{ISS}$ for the ISS-images, to avoid noise. We estimated the selected range for each dataset based on visual inspection of the data, by comparing patterns within each plot. Each linear fit was computed by fitting an ordinary least square fit to the

data with equal weights.

5.3.1 GMT256 Halo Profile

The computed linear fits of the log-transformed data for GMT256 in each color-band, see Figure 5.10.

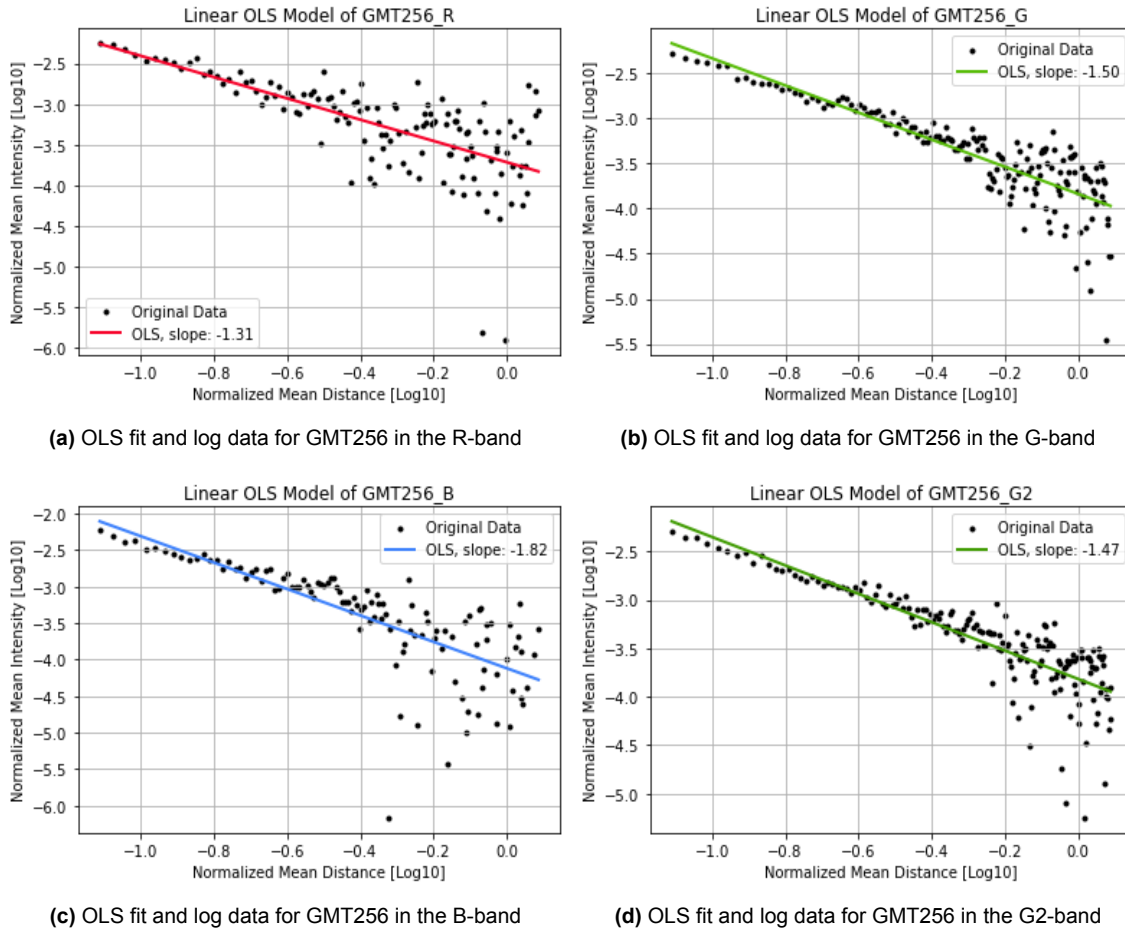
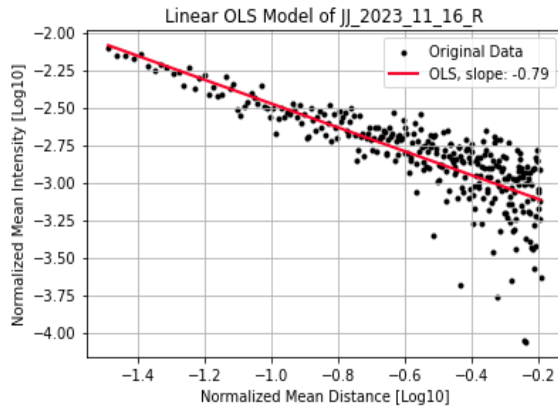


Figure 5.10: The computed best fit linear OLS fit along the normalized data for each color-band of GMT256 with logarithmic axes. Each linear fit of GMT256 for each color-band was computed within a distance of approximately $[0.08R_{ISS}; 1.26R_{ISS}]$.

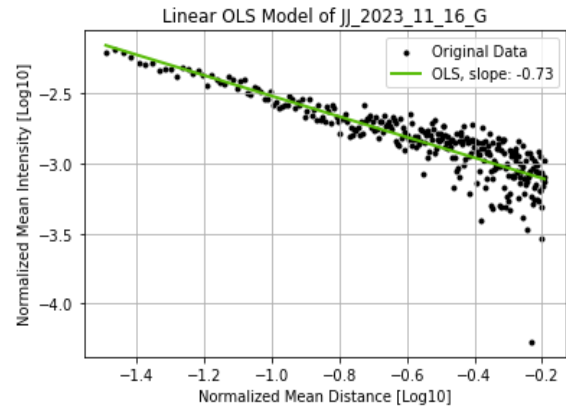
As shown in Figure 5.10, variations in slope are observed across different colors. Specifically, the R-band exhibits the smallest slope, as depicted in Figure 5.10a, while the B-band displays the largest slope, as illustrated in Figure 5.10c. The green color bands have similar slopes see Figure 5.10b and Figure 5.10d.

5.3.2 JJ16 Halo Profile

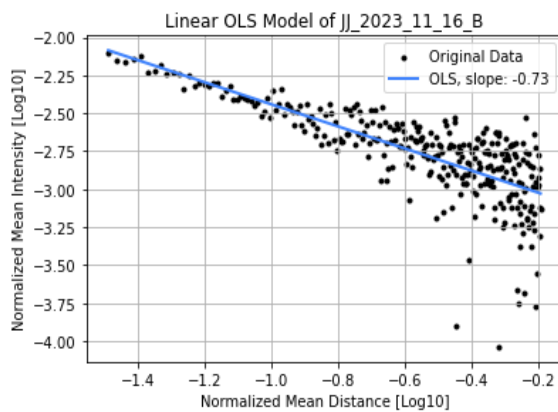
The computed linear fits of the log-transformed data for JJ16 in each color-band, see Figure 5.11.



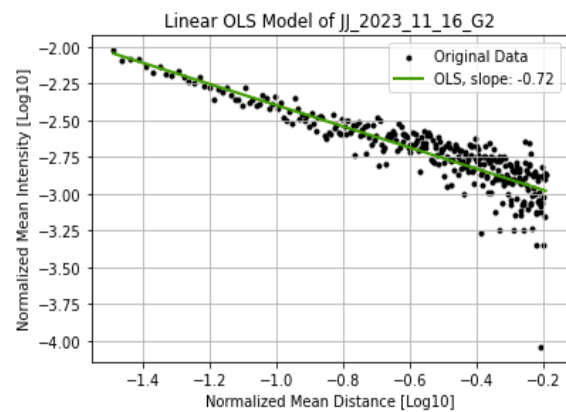
(a) OLS fit and log data for JJ16 in the R-band



(b) OLS fit and log data for JJ16 in the G-band



(c) OLS fit and log data for JJ16 in the B-band



(d) OLS fit and log data for JJ16 in the G2-band

Figure 5.11: The computed best fit linear OLS fit along the normalized data for each color-band of JJ16 with logarithmic axes. Each linear fit was computed for data within a distance of approximately $[0.03R_{JJ}; 0.63R_{JJ}]$.

The R-band displays the largest slope, as illustrated in Figure 5.11a. The slopes of the B, G and G2-band are similar, see Figure 5.11c, Figure 5.11b and Figure 5.11d.

5.3.3 JJ15 Halo Profiles

The computed linear fits of the log-transformed data for JJ15 in each color-band is seen in Figure 5.12.

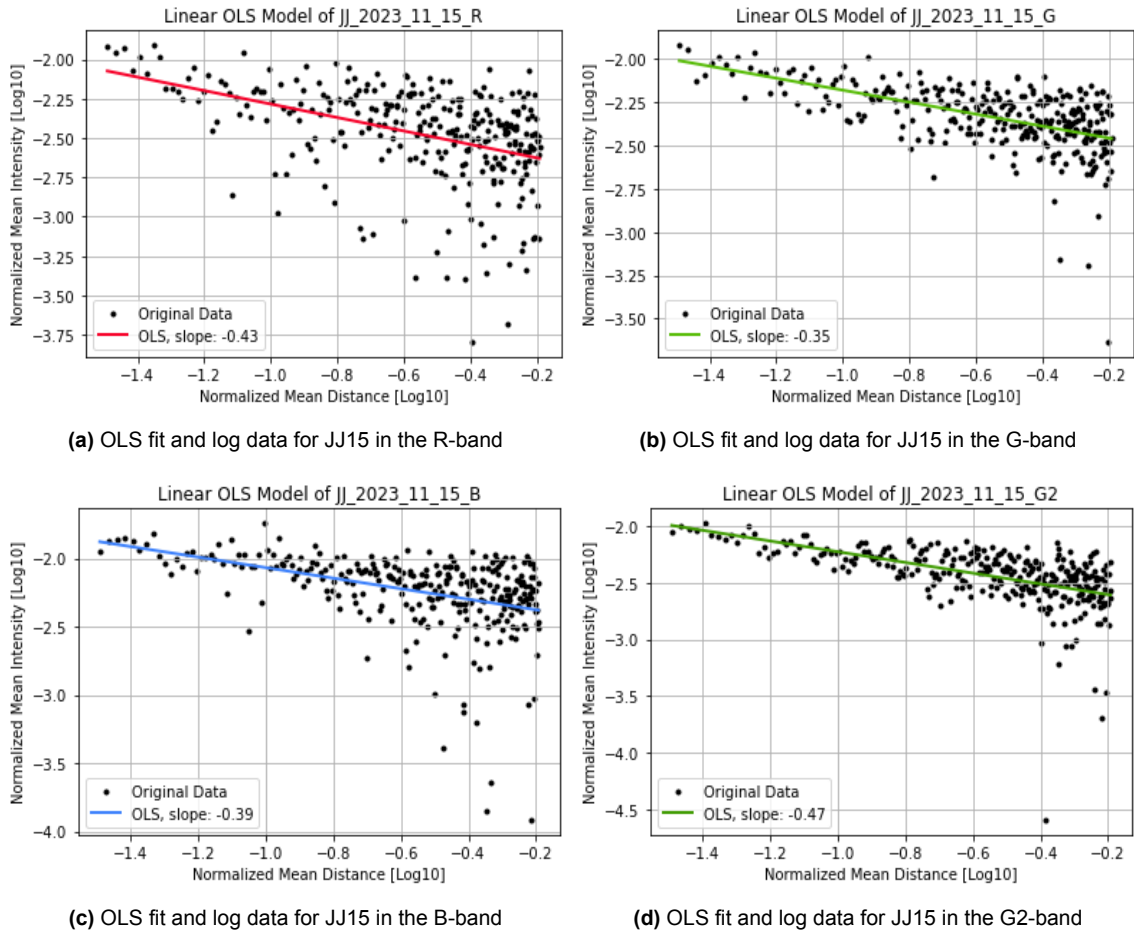
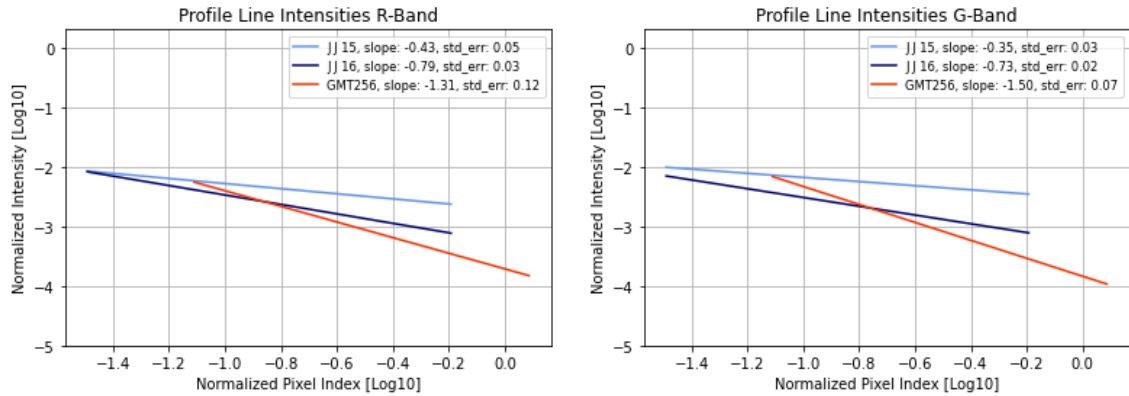


Figure 5.12: The computed best fit linear OLS fit along the normalized data for each color-band of JJ15 with logarithmic axes. Each linear fit was computed for data within a distance of approximately $[0.03R_{JJ}; 0.63R_{JJ}]$.

The computed linear fit of JJ15 has more fluctuations in the measured data in contrast to JJ16, see Figure 5.11. We also observe higher levels of noise for G compared to G2, in addition, the slope of G is smaller than the other color-bands, including G2.

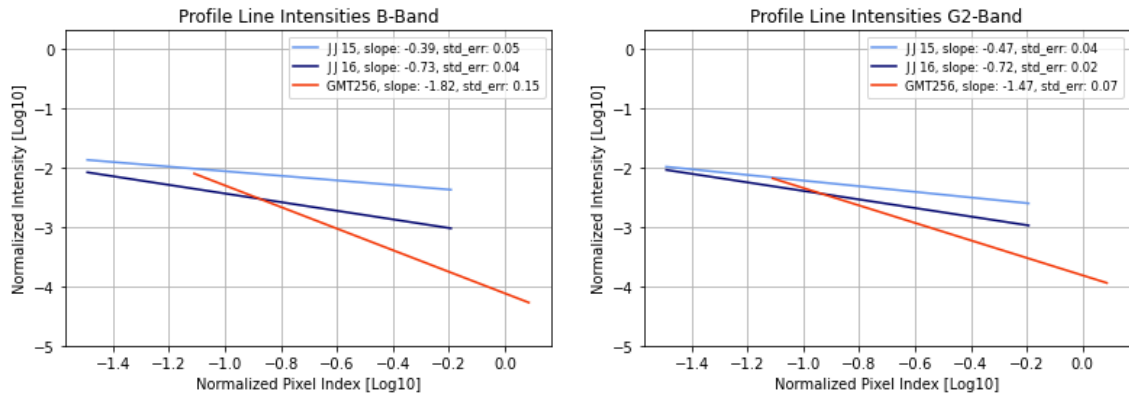
5.3.4 Linear Fit Comparison

The resulting linear fits were obtained by *ordinary least square* method for each dataset: GMT256, JJ15 and JJ16 grouped by color-bands, as shown in Figure 5.13.



(a) The R-band slopes of GMT256 (red), JJ15 (light blue) and JJ16 (navy blue).

(b) The G-band slopes of GMT256 (red), JJ15 (light blue) and JJ16 (navy blue).



(c) The B-band slopes of GMT256 (red), JJ15 (light blue) and JJ16 (navy blue).

(d) The G2-band slopes of GMT256 (red), JJ15 (light blue) and JJ16 (navy blue).

Figure 5.13: Linear OLS fits of the GMT256 (red), JJ15 (light blue) and JJ16 (navy blue) data for each color-band. Each figure compares the linear fit grouped by color-bands; the derived slopes and standard error are shown in each figure's legend (top right).

Figure 5.13 shows GMT256 has the largest slope across all color-band compared to those from Earth, followed by the JJ16 dataset and the smallest slopes are seen for the JJ15 dataset. In contrast, we see larger errors from the calculated standard deviation of the linear fit for GMT256 compared to the rest.

It's also shown, that when comparing the ISS profiles to those from Earth, the largest difference is in the B-band profile and the smallest difference is seen in the R-band. Meanwhile, differences between slopes of the Earth data are seen in different color-bands. To test if the differences are significant, we calculate Z using the slopes and standard errors of the linear fits for images in the corresponding color-bands and compare them to a significance of $Z = 2$, see subsection 4.4.2.

The calculated differences between each dataset as shown in Table 5.3 and Table 5.6 using Z .

GMT256	slope	std_err	JJ15 [Z]	JJ16 [Z]
R	-1.31	0.12	-6.56	-4.03
G	-1.50	0.07	-14.98	-10.42
G2	-1.47	0.07	-12.25	-10.15
B	-1.82	0.15	-9.21	-7.18

Table 5.3. Slope and standard error for the linear fits of GMT256 in each color-band and the calculated Z of GMT256 compared to JJ15 and JJ16 of the corresponding color-bands.

Table 5.3 shows the slopes of the OLS fits for GMT256 and the affiliated standard error for each color-band, the columns *error JJ15* and *error JJ16* is the difference between the slopes weighted by the standard errors Z. We see a significant difference in slope when comparing JJ15 and JJ16, the slope of GMT256 is significantly more negative compared to the other. The largest difference is found for GMT256 and JJ15 for all color-bands.

JJ15	slope	std_err	JJ16 [Z]	JJ16	slope	std_err	JJ15 [Z]
R	-0.43	0.05	5.89	R	-0.79	0.03	-5.89
G	-0.36	0.03	10.17	G	-0.73	0.02	-10.17
G2	-0.47	0.04	5.27	G2	-0.72	0.02	-5.27
B	-0.39	0.05	5.61	B	-0.73	0.04	-5.61

Table 5.4. Slope, standard error and Z for JJ15. **Table 5.5.** Slope, standard error and Z for JJ16

Table 5.6. Slope, standard error and Z for the linear fits of JJ15 (left) and JJ16 (right) in each color-band.

The comparison between each Earth dataset from Jens Jacobsen illustrated in Table 5.6 also shows a significant difference between the two images at different dates. The slope of the image combined JJ16 from the 16th of November 2023 is more negative than the image JJ15 from the 15th of November 2023, and the largest difference is for the G-band.

[Z]	G - G2	G - R	G - B	R - B	G2 - B	G2 - R
GMT256	-0.37	-1.35	1.90	2.62	2.13	-1.10
JJ15	2.37	1.23	0.55	-0.59	-1.39	-0.69
JJ16	-0.22	1.63	-0.02	-1.37	0.14	1.80

Table 5.7. Comparison of slopes between color-bands within the same image given as Z.

Lastly, we compared the slopes and standard errors of the linear fit between each color-band within a dataset (the different colors of the same image), see Table 5.7. GMT256 has larger contrasts between the G and R, G and B, R and B, and the G2 and B color-bands. Both GMT256 and JJ16 did not show significant differences between G and G2, in contrast for JJ15 we observed a significant difference between G and G2.

6 Discussion

In this study, we aimed to analyze the halo profile of the Moon to understand the extent to which scattered light is reduced when observing from space. We developed a method for processing the images for data reduction and implemented a technique for aligning images that have been rotated and shifted before image averaging to decrease noise. Furthermore, we analyzed the halo profile of the Moon from images taken from the ISS and Earth and calculated the Z scores for the linear fits.

From our analysis of the halo profiles in images taken by Andreas Mogensen and Jens Jacobsen, we observed significant differences in the slopes of the fits across the color bands. Specifically, the image data from GMT256 exhibited significantly more negative slopes for all color bands compared to those from JJ16 and JJ15.

It is important to note, that the residuals representing the difference between the measured profiles and linear fits might not be independent and identically distributed. This consideration means that using a significance value of $Z=2$ might have been overly ambitious, as it corresponds to a 5% chance of error. The results of our analysis must be interpreted cautiously. With a more fitting Z , the differences in color-band slopes for individual images might be deemed insignificant, but the differences between the slopes of ISS and Earth images in corresponding color bands could still be significant. To draw definitive conclusions about the significance, further analysis and improvements of the experiment are necessary.

6.1 Methods - Data Reduction

The filter was effective in reducing the amount of images by removing invalid data and saving images that would otherwise have been rejected. However, we did observe a few *false negatives*. The overall efficiency of the filter made it possible to save more images to optimise noise reduction. Filtering RAW images before separating them into color bands may have excluded images that were not overexposed in specific color bands. However, this approach ensured that we had equal amounts of each color-band image for each dataset, allowing for consistent comparisons.

The filter saved 42 images in GMT009, 70 images in GMT039 and 80 images in GMT256, see Table 5.1. The filter found no potentially over-exposed images from Jens Jacobsen, the resulting images contained no pixels with maximum values.

An interesting observation was that the saved images only contained small amounts of hot pixels and overexposed images always contained more than at least 40 pixels. Future improvement of the filter would include only investigating images containing fewer than 10 pixels at maximum intensity.

6.2 Method - Alignment And Averaging

A crucial step was to align the images, to create a combined average image, increasing the SNR. Initially, we did not use the same reference image for each color-band when aligning images from GMT009, GMT039, JJ15 and JJ16, this was corrected for GMT256. The inconsistency of reference images might have affected the profile of Jens' images.

The method might have accidentally introduced noise when aligning the images. This could have been avoided by additional processing to remove hot pixels before alignment. Despite this, the additional noise levels were reduced, when creating the average image.

At length, the shift in the placement of the ghost images was not accounted for, when aligning the images. This could affect the region of measurement, by scattering the ghost images. In addition, we did not check for blurred images, which also affects the final combined image. To avoid errors from misalignment and additional light from sources discussed above, we removed sections of each profile to prevent bias. Improvements would consist of the removal of hot pixels before alignment and secondly, implementing validation procedures to ensure only similar images are used.

6.3 ISS images - Ghost Images

The images captured from the ISS were taken from within the cupola module, requiring the Moon to be photographed through a thick window, introducing additional optical phenomena beyond those discussed in subsection 2.4.2. The ghost images were caused by internal reflections and the angle at which the light entered the window. Dust and imperfections cause scattering, this could affect the ISS images, as we have seen images revealing small imperfections on the glass caused by the harsh space environment, discussed in subsection 2.4.2.

Despite having received large amounts of image data from the ISS, only one dataset of images *GMT256* was suitable for analyzing the halo profile with the current methods. We excluded data from *GMT009* and *GMT039* due to a significant amount of ghost images (reflected images of the *crescent*) interfering with the measurements. We also observed ghost images sometimes appearing blurred.

Interestingly, *GMT256* exhibited a different pattern and location of ghost images compared to *GMT009* and *GMT039*. In *GMT256*, the placement of ghost images did not intersect with the area of measurement, making it suitable for analysis. The images from *GMT256* were more compatible with the images from *JJ15* and *JJ16*, as these were taken only 5-6 days apart. In addition, the illumination of the Moon was also within a reasonable range as the Moon was at each side of the phase *New*, see Table 3.1.

6.4 Halo Profile Analysis

The findings of Table 5.3 did reveal significant differences according to $Z = 2$, in the slopes of the linear fits for comparisons between the images from Andreas and Jens. We also observed significant differences in Jens's images, despite being photographed 1 day apart.

Interestingly, a deviation between the two green color-bands within the same image *JJ15* in contrast to *JJ16*, despite detecting the same wavelengths. Next, we did find significant differences between the red and blue color-bands for *GMT256*. This might be due to the behaviour of the Airy disc being dependent on wavelength.

Jens Jacobsen's images show less contrast, this may be caused by the atmosphere. According to mie scattering, wavelengths are scattered equally as mentioned in subsection 2.4.1. Subsequently, the influence of mie scattering on the profile could vary according to the date, as the scattering depends on the airmass and atmospheric properties. We did not use the same reference image per dataset when aligning the images, this affected the length of the profile for each color-band within an image. At length, none of the images were corrected using flat-fields, potentially impacting the slopes. Despite not correcting the images, we did implement changes when extracting the mean background pixel intensity to reduce potential curvature and vignetting, by avoiding the image corners and only using values centered at the borders.

The length of the profile was also restricted by the Moon-to-frame ratio. We were not able to measure far enough to reach pixels with intensities equal to the background for Jens'

images, unlike Andreas' images. Despite this limitation, the slopes of the linear fit should remain unaffected, as we expect the relationship to be linear.

It was not possible to fit a linear model within the same range of Normalized distances *Normalized pixel index* for both Jens and Andreas' images, as the linear graph was not compatible with the data.

In our analysis, we found a significant difference between JJ15 and JJ16 in the green color-band. The images from JJ15 exhibited higher noise levels compared to those from JJ16 across all color-bands, see Appendix B. The comparison of JJ15 to JJ16, with the linear fit next to the data plotted with the error bound derived from the profile intensity of the individual measurement is illustrated in Figure 6.1.

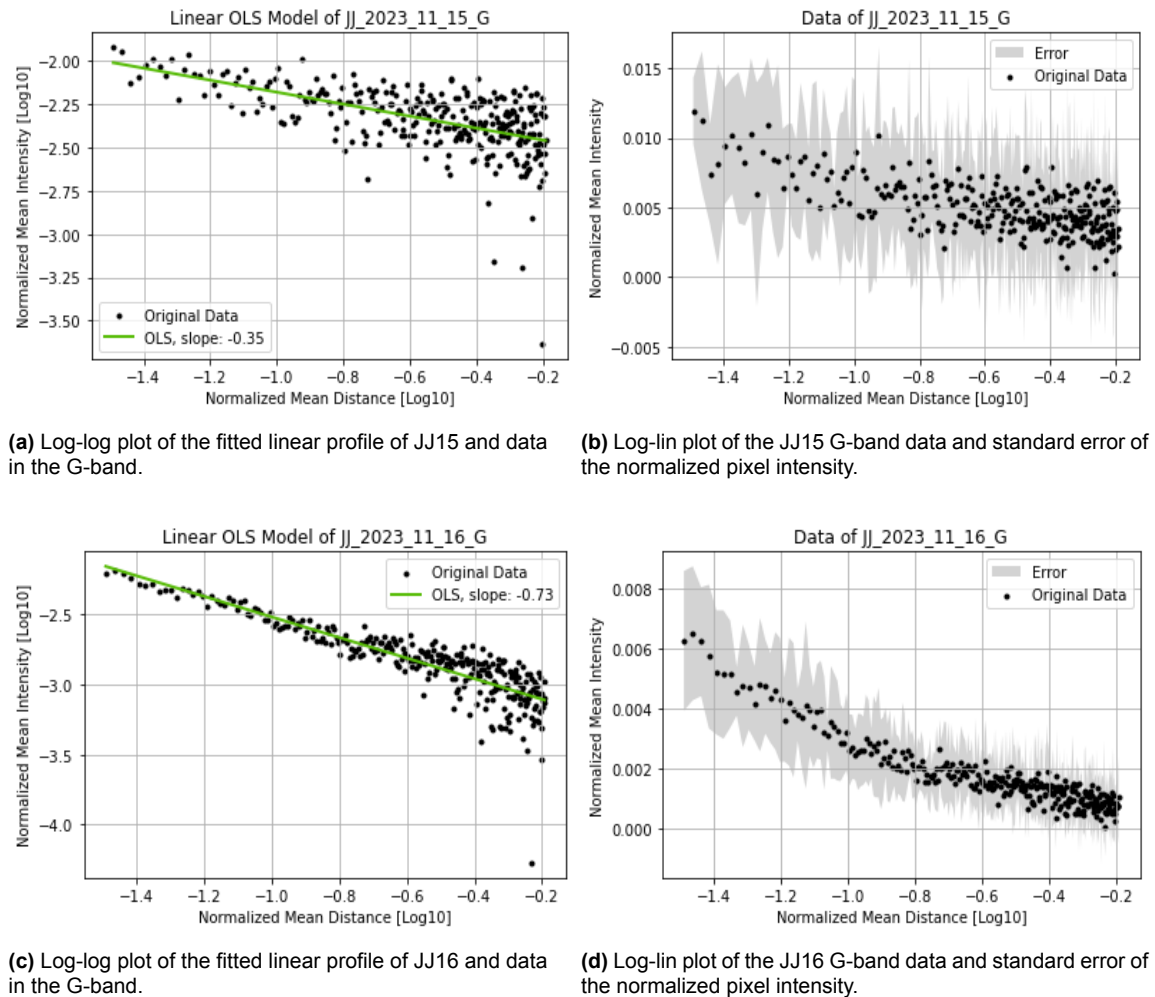


Figure 6.1: The figures show the comparison of the estimated linear fit of the two images JJ15 (a) and JJ16 (c) from Jens Jacobsen in the G-band and the data including the standard deviation of each profile intensity of JJ15 (b) and JJ16 (d). Note the different scales for each figure.

The disagreement between the two images from Jens Jacobsen could be caused by several factors and the combined effects ranging from each step of the processing to observatory conditions, including varying noise levels and sparse data. The average image of JJ15 was composed of fewer images than JJ16, this could affect the noise level. Then there is the possibility of differences according to incorrect exposure and atmospheric

disturbance. From the metadata of the images, we found camera temperatures of 35 Celcius.

To summarise, our analysis demonstrates the potential of space-based observations to remove atmospheric interference. Although the study was affected by limitations regarding data and optical distortions, the experiment provided a foundation for future research.

7 Future Work

Despite obstacles, the results of the data analysis showed promising prospects for future experiments and applications to investigate the influence of the atmosphere on Moon observations to improve the Earthshine method.

Future work would include the improvement of the image processing software developed in this project to reduce bias and errors produced by the current methods and to optimise the script. The improvements would consist of implementing methods for avoiding underexposed images and object detection. Further, the removal of defects such as cosmic rays and hot pixels by smoothing the images using filters, additionally incorporating flatfield and dark field corrections to reduce bias and noise. Also, be able to process the reflected images.

For future analysis, more compatible linear fits of the halo profile must be used to reduce bias for comparisons between Earth- and space-based observations. This would include using images of similar moon-to-frame ratios to prevent cutoff and linear fits of the corresponding region of the halo. Also, optimize methods to obtain the halo profiles during image analysis by using additional extraction methods.

Furthermore, improvement upon how the image data from the ISS is collected to minimize optical distortions such as ghost images and blurring. At length, new methods for controlling the movement of the photographer for diminishing the rotation and translation of the Moon between images.

This could be achieved by limiting the amount of light allowed to enter the camera using a cover and a mount fixed to the inner structure of the Cupola module.

Also implementing image processing methods to reduce or remove ghost images before alignment and image averaging. One suggestion is to reconstruct the ghost images and then subtract them from the images. Also analysing the reflected images of the crescent to find the order of magnitude. Lastly, to investigate the cause and patterns, by reconstruction of the experiment in a lab.

8 Conclusion

In this study, we aimed to compare the halo profile of the Moon by analyzing images taken from the International Space Station and Earth-based observations to understand the impact of the atmosphere and provide valuable insights to improve the Earthshine method.

The findings of our analysis of the halo profile and comparison of linear fits revealed that images from space exhibited different patterns compared to images from Earth. Further, we found significant differences in the slopes of the linear fits, showing a larger negative slope of the halo profile of Andreas Mogensen's images compared to those from Jens Jacobsen, yielding a larger contrast between the bright side of the moon and the background.

The results provide promising knowledge for improving the Earthshine method to better the contrast used to determine the planetary albedo, when observing in the absence of an atmosphere, thus removing the problem of mie scattering and atmospheric interference.

However, the constraints of this study included limitations of suitable images from the ISS, despite large amounts of data. The presence of ghost images by the windows of Cupola reduced the available data to one dataset. As a consequence, we were not able to compare different days of image data from the ISS. In addition, the windows might have influenced the results along with the methods applied when processing the images. Meanwhile, varying atmospheric conditions and processing errors might have affected the results of the earth-based observations.

Future research would include the improvement of the observation technique and the implementation of advanced image processing to reduce optical distortions and displacement in images from the ISS. Also, the analysis would benefit from modifications of the used techniques for filtering and alignment of the image data, and additional image processing to include errors from the camera. At length, optimize the compatibility of images used for comparing halo profiles.

In conclusion, the analysis of Andreas Mogensen's moon images highlights the potential of space-based observations to improve the Earthshine method in the context of climate research.

Bibliography

- [1] ESA. *Illuminating Earth's shine*. Accessed 31th May 2024. URL: https://www.esa.int/Science_Exploration/Human_and_Robotic_Exploration/Illuminating_Earth_s_shine.
- [2] ESA. *Climate science in orbit*. Accessed 1th June 2024. URL: https://www.esa.int/Science_Exploration/Human_and_Robotic_Exploration/Climate_science_in_orbit.
- [3] Jens Olaf Pepke Pedersen. *Kompendium, Geo- og Planetfysik II, Kursus 30142*. 2023.
- [4] P. R. Goode et al. "Earth's Albedo 1998–2017 as Measured From Earthshine". In: *Geophysical Research Letters* 48.17 (2021). e2021GL094888 2021GL094888, e2021GL094888. DOI: <https://doi.org/10.1029/2021GL094888>. eprint: <https://agupubs.onlinelibrary.wiley.com/doi/pdf/10.1029/2021GL094888>. URL: <https://agupubs.onlinelibrary.wiley.com/doi/abs/10.1029/2021GL094888>.
- [5] Henriette Schwarz. "Photometric Characterization of the Earthshine Telescope". In: 2012. URL: <https://api.semanticscholar.org/CorpusID:119985560>.
- [6] J. Qiu et al. "Earthshine and the Earth's albedo: 1. Earthshine observations and measurements of the lunar phase function for accurate measurements of the Earth's Bond albedo". In: *Journal of Geophysical Research: Atmospheres* 108.D22 (2003). DOI: <https://doi.org/10.1029/2003JD003610>. eprint: <https://agupubs.onlinelibrary.wiley.com/doi/pdf/10.1029/2003JD003610>. URL: <https://agupubs.onlinelibrary.wiley.com/doi/abs/10.1029/2003JD003610>.
- [7] Frank L. Pedrotti, Leno M. Pedrotti, and Leno S. Pedrotti. *Introduction to Optics*. 3rd ed. Cambridge University Press, 2017.
- [8] Rasmus Reinhold Paulsen and Thomas B. Moeslund. *Introduction to Medical Image Analysis*. English. 1. Undergraduate Topics in Computer Science. Germany: Springer, 2020. ISBN: 978-3-030-39363-2. DOI: 10.1007/978-3-030-39364-9.
- [9] Glenn H. Chapman et al. "Single Event Upsets and Hot Pixels in digital imagers". In: *2015 IEEE International Symposium on Defect and Fault Tolerance in VLSI and Nanotechnology Systems (DFTS)*. 2015, pp. 41–46. DOI: 10.1109/DFT.2015.7315133.
- [10] William C. Porter et al. "Dark current measurements in a CMOS imager". In: *Sensors, Cameras, and Systems for Industrial/Scientific Applications IX*. Ed. by Morley M. Blouke and Erik Bodegom. Vol. 6816. International Society for Optics and Photonics. SPIE, 2008, p. 68160C. DOI: 10.1117/12.769079. URL: <https://doi.org/10.1117/12.769079>.
- [11] Michael Wulf Friedlander. *cosmic ray*. Accessed 13 April 2024. 2024. URL: <https://www.britannica.com/science/cosmic-ray>.
- [12] Stéfan van der Walt et al. "scikit-image: image processing in Python". In: *PeerJ* 2 (June 2014), e453. ISSN: 2167-8359. DOI: 10.7717/peerj.453. URL: <https://doi.org/10.7717/peerj.453>.
- [13] Maik Riechert. *rawpy 0.21.0*. Accessed 2th June 2024. URL: <https://pypi.org/project/rawpy/>.
- [14] *About LibRaw*. Accessed 30th May 2024. URL: <https://www.libraw.org/>.
- [15] R.C. Gonzalez and R.E. Woods. *Digital Image Processing*. Pearson, 2018. ISBN: 9780133356724. URL: <https://books.google.dk/books?id=0F05vgAACAAJ>.

- [16] B.S. Reddy and B.N. Chatterji. "An FFT-based technique for translation, rotation, and scale-invariant image registration". In: *IEEE Transactions on Image Processing* 5.8 (1996), pp. 1266–1271. DOI: 10.1109/83.506761.
- [17] Stéfan van der Walt et al. *Register rotation and scaling on a translated image - Part 2*. Accessed 20th May 2024. 2024. URL: https://scikit-image.org/docs/stable/auto_examples/registration/plot_register_rotation.html#using-polar-and-log-polar-transformations-for-registration.
- [18] Tim Kazik and Ali Göktoğlan. "Visual odometry based on the Fourier-Mellin transform for a rover using a monocular ground-facing camera". In: Apr. 2011, pp. 469–474. ISBN: 978-1-61284-982-9. DOI: 10.1109/ICMECH.2011.5971331.
- [19] Skipper Seabold and Josef Perktold. "statsmodels: Econometric and statistical modeling with python". In: *9th Python in Science Conference*. 2010.
- [20] K. McGuffie and A. Henderson-Sellers. *A Climate Modelling Primer*. John Wiley Sons Ltd, 1997.

A Energy budget

A.1 Energy budget and balance

The global mean effective temperature T_{eff} is determined by the flow of energy. For the temperature to be stable over long periods the energy budget at the top of the atmosphere must be in balance. The incoming radiation at the top of the atmosphere is defined as the Total Solar Irradiance (TSI) also noted as the solar constant S . This is the average amount of total incoming energy times the cross-sectional surface πR_e^2 projected onto the sky and the albedo.

$$E_{in} = (1 - A_p)S\pi R_e^2 \quad (\text{A.1})$$

Where R_e is the radius of the Earth and A_p is the planetary albedo described in subsection 2.2.1. As some of the incoming flux is reflected back by the atmosphere, whereas the rest is absorbed - approximately 70% [3].

For simplicity, the Earth is treated as a black body and the absorbed energy is re-emitted as thermal energy following Stephan-Boltzmann law. The incoming heat flux must be equal to the outgoing heat loss to balance the system yielding.

$$E_{out} = 4\pi R_e^2 \sigma T_{eff}^4 \quad (\text{A.2})$$

The outward flux is assumed uniformly emitted across the whole surface area. σ is the Stephan-Boltzmann constant and T_{eff}^4 is the effective temperature. The effective temperature is defined as the theoretical temperature of a black body, required to keep the system in balance. Assuming energy balance, the terms of incoming (??) and outgoing energy (A.2) yields.

$$\begin{aligned} E_{in} &= L_{out} \Leftrightarrow \\ T_{eff}^4 &= \frac{S}{4\sigma}(1 - A_p) \end{aligned} \quad (\text{A.3})$$

(A.3) expresses the effective temperature of the system in terms of the solar constant S , σ being the Stephan-Boltzmann constant and the planetary albedo A_p . While T_{eff} is the simplified term of Earth's theoretical temperature, the expression clearly depicts the importance of the albedo.

A.2 Surface and atmosphere energy budget

A more realistic expression regarding Earth's energy budget must account for the atmosphere and greenhouse effect, as they contribute to the system's temperature. Even though most of the incoming radiation is absorbed by the surface, meanwhile the atmosphere is almost transparent to the visible range of the electromagnetic spectrum absorbing only 20%. A significant fraction of the re-emitted thermal energy is absorbed by the atmosphere as it is opaque to the majority of infrared. Greenhouse gasses in the atmosphere such as water vapour, carbon dioxide, methane and ozone absorb and re-emit the energy, increasing the temperature of the system.

For an atmosphere containing greenhouse gasses, the surface temperature T_s becomes larger than the effective temperature. As the effective temperature is equal to the atmospheric T_a when assuming one homogeneous layer the radiant exitance becomes.

$$\sigma T_{eff}^4 = \frac{1}{4}(1 - A_p)S = \sigma T_a^4 \quad (\text{A.4})$$

Yielding a higher surface temperature because of the greenhouse effect:

$$\sigma T_s^4 = \frac{1}{4}(1 - A_p)S + \sigma T_a^4 \quad (\text{A.5})$$

Accounting for greenhouse gasses in Earth's atmosphere raising the surface temperature an additional expression describing the effect is $T_s = T_{eff} + \Delta T$. Where ΔT is the greenhouse increment and is dependent on the efficiency of the infrared absorption [20]. Further introducing the greenhouse forcing parameter G as the difference between the emission at the top of the atmosphere described by [6].

$$G = \sigma(T_s^4 - T_{eff}^4) \quad (\text{A.6})$$

The normalized greenhouse effect g is written in terms of the temperature difference because of its dependence on the top of the atmosphere outgoing- and surface long-wave radiation.

$$\begin{aligned} g &= G/\sigma T_s^4 \Leftrightarrow \\ T_{eff}^4 &= (1 - g)T_s^4 \end{aligned} \quad (\text{A.7})$$

Additionally, G is proportional to the amount of greenhouse gasses as we recall the expression of the greenhouse increment ΔT . Now, the effective temperature of the outgoing flux is written in terms of the surface temperature T_s and normalized greenhouse effect by substituting (A.7) into (A.2).

$$L_{out} = 4\pi R_e^2(1 - g)\sigma T_s^4 \quad (\text{A.8})$$

Finally the energy balance $E_{in} = L_{out}$ yields

$$T_s^4 = \frac{S}{4\sigma(1 - g)}(1 - A_p) \quad (\text{A.9})$$

Considering the expression above (A.9), the relation between the mean surface temperature T_s and the planetary albedo A_p .

B Results - All halo profiles

B.1 Data and standard deviation

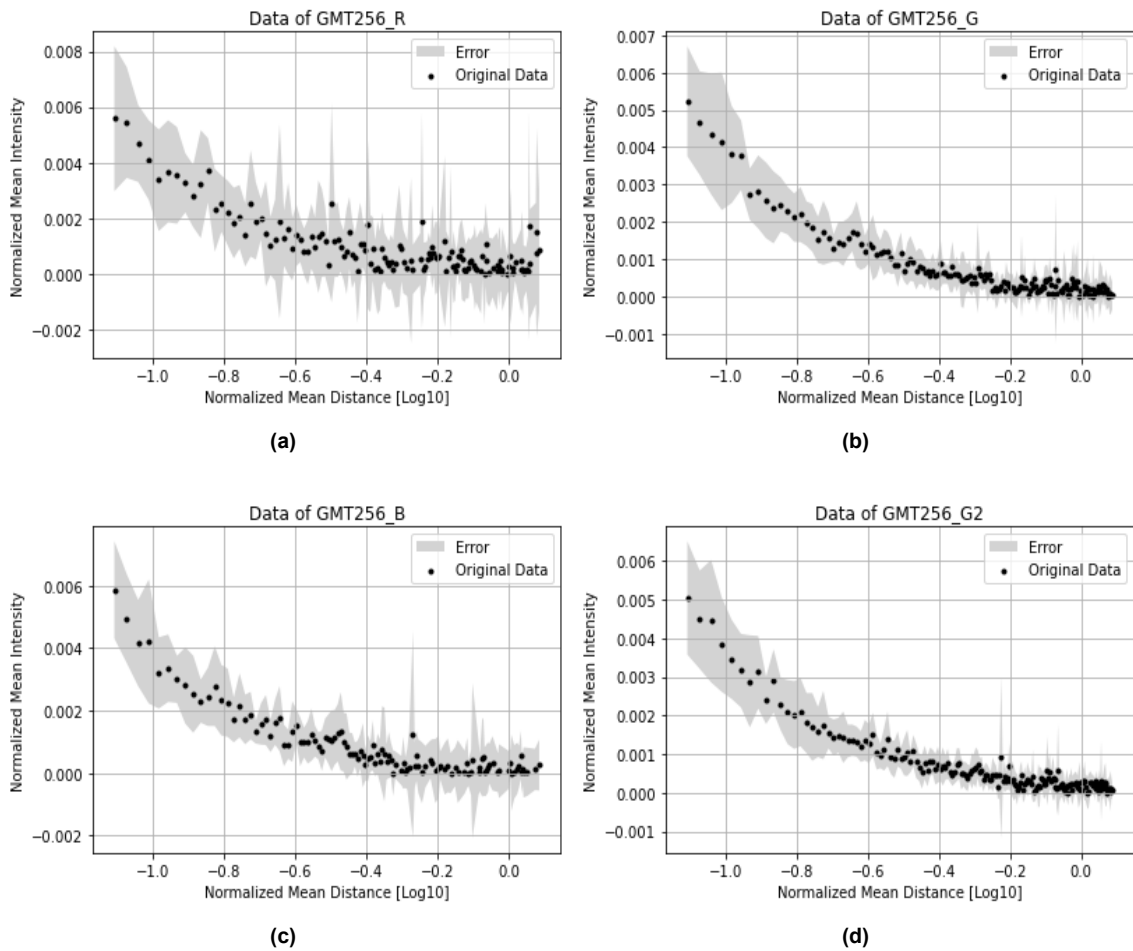
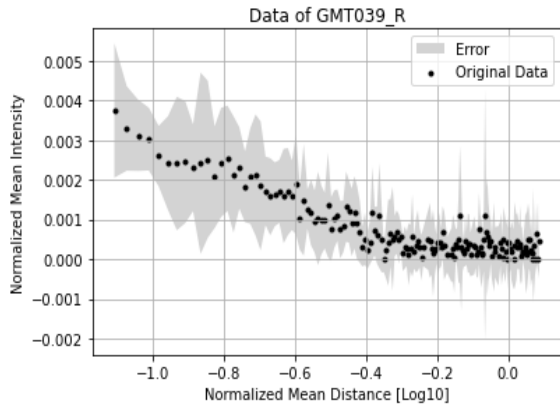
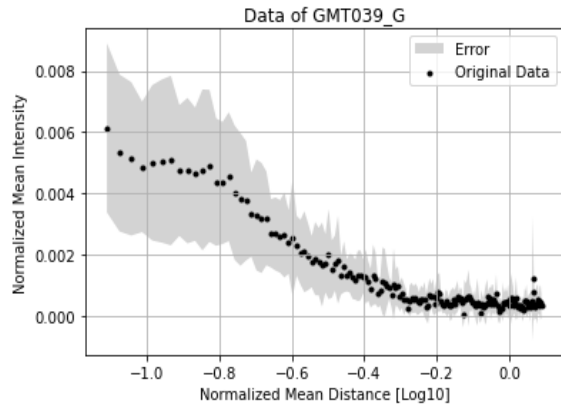


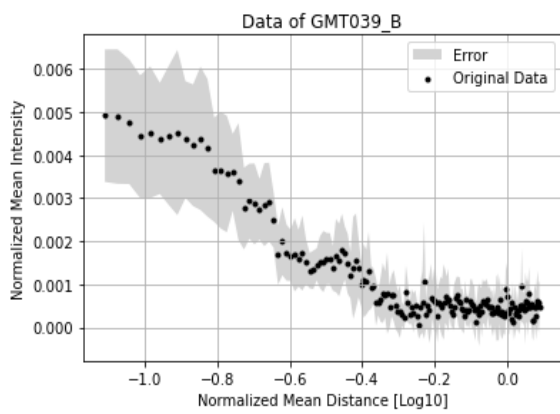
Figure B.1:



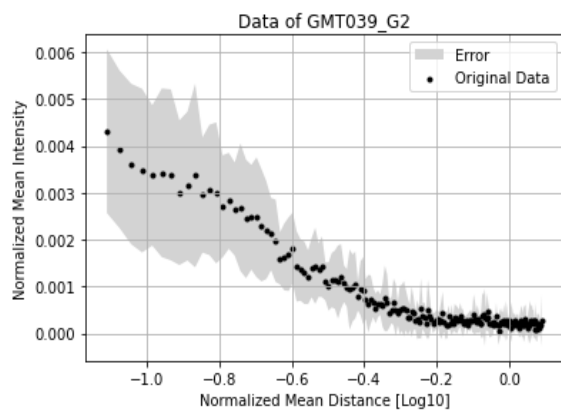
(a)



(b)

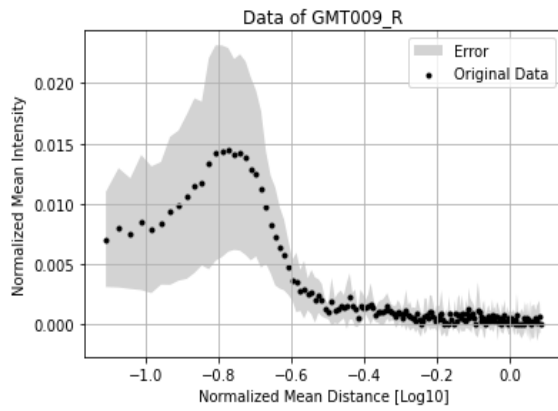


(c)

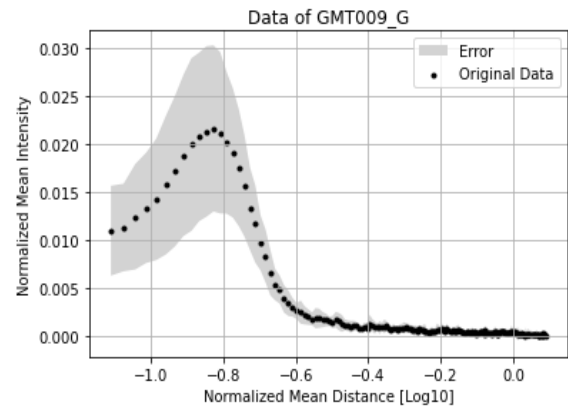


(d)

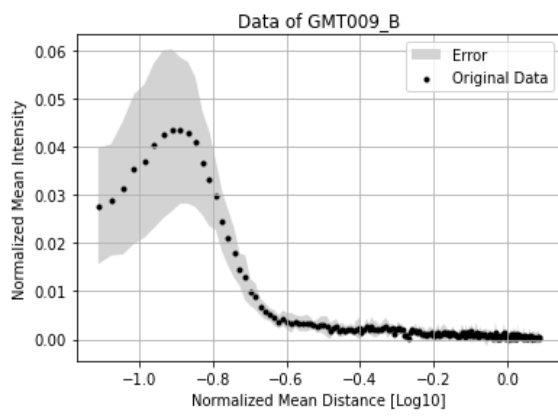
Figure B.2:



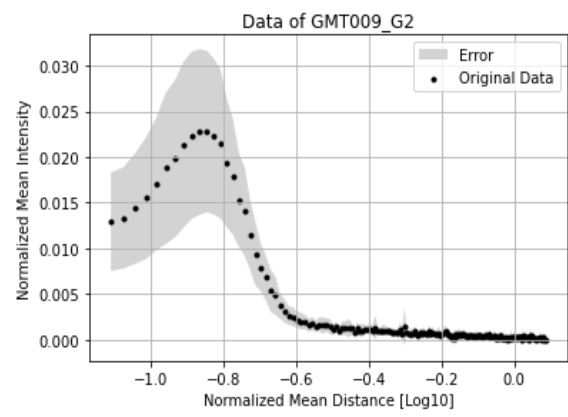
(a)



(b)

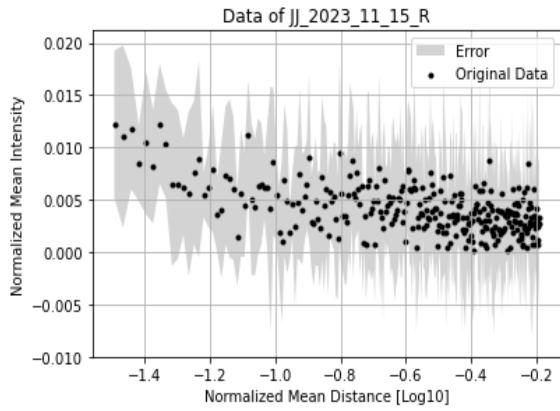


(c)

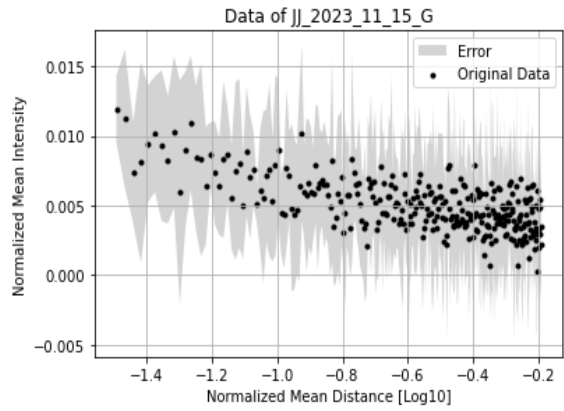


(d)

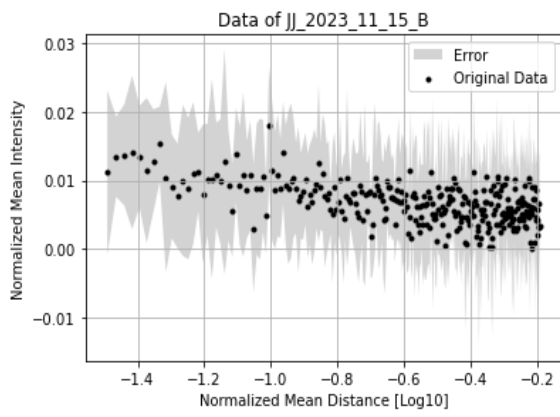
Figure B.3:



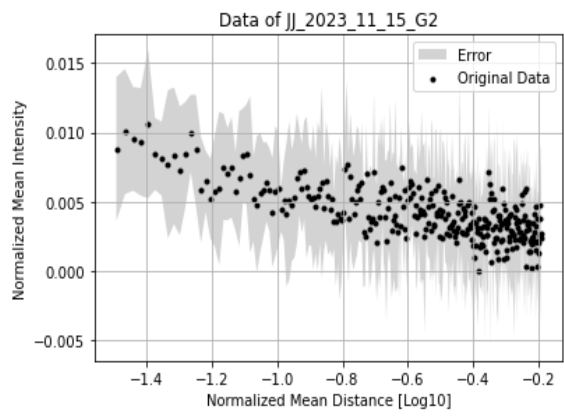
(a)



(b)

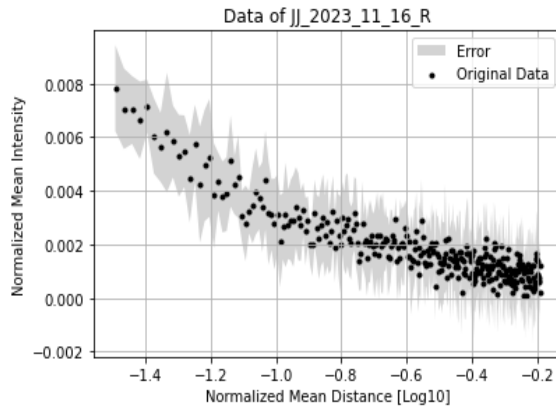


(c)

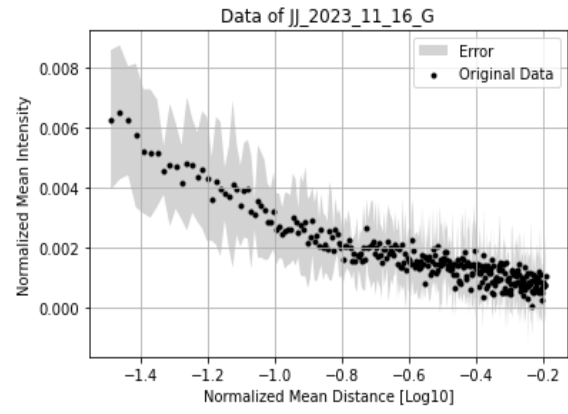


(d)

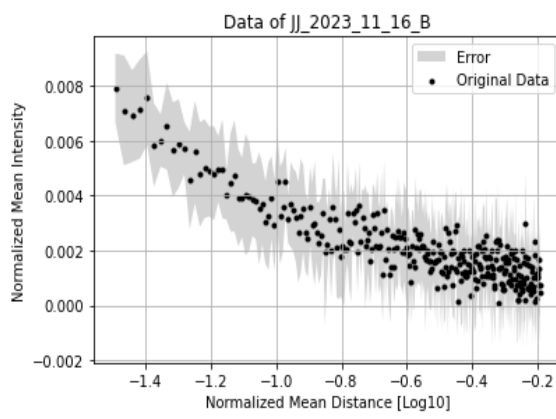
Figure B.4:



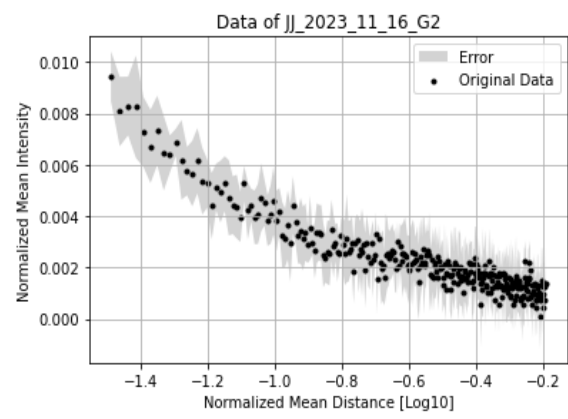
(a)



(b)



(c)



(d)

Figure B.5:

B.1.1 OLS linear fit of GMT256

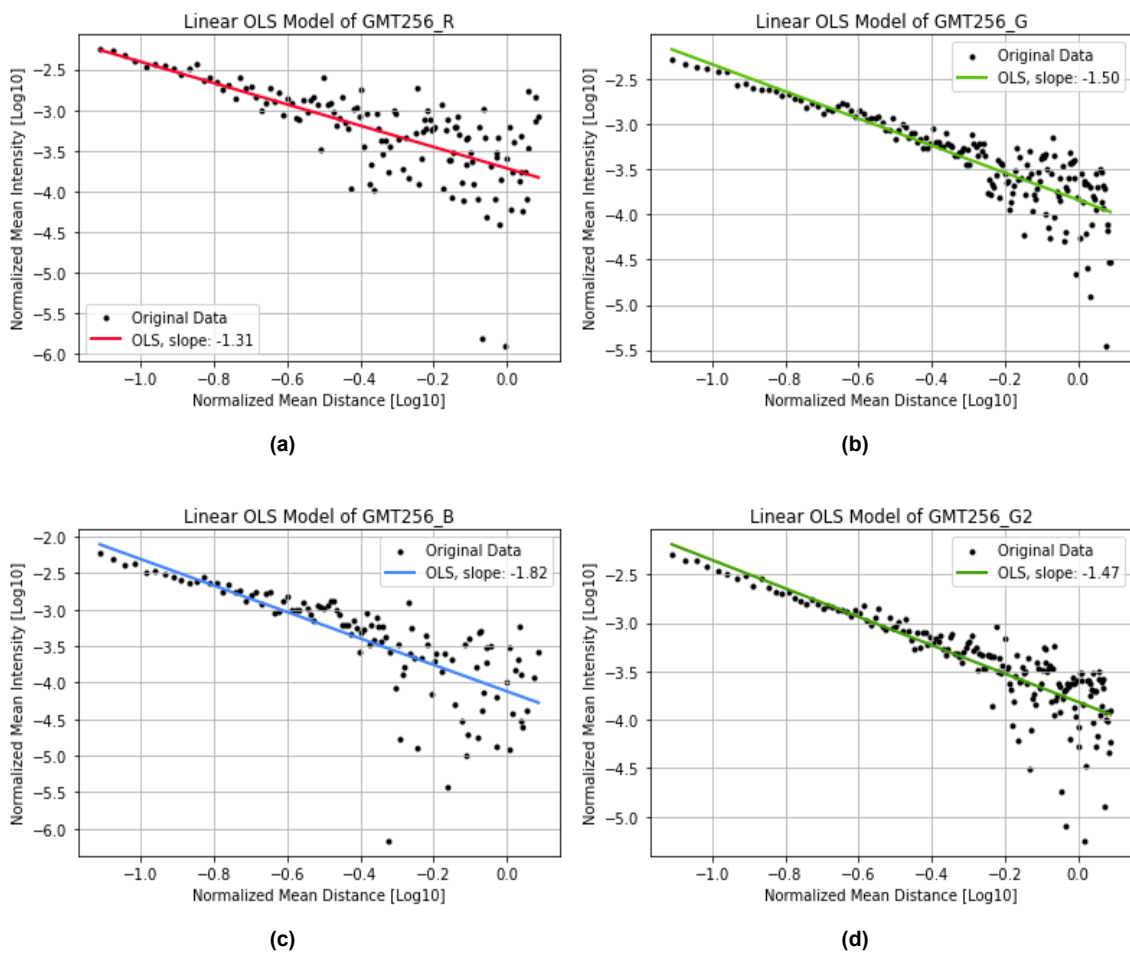
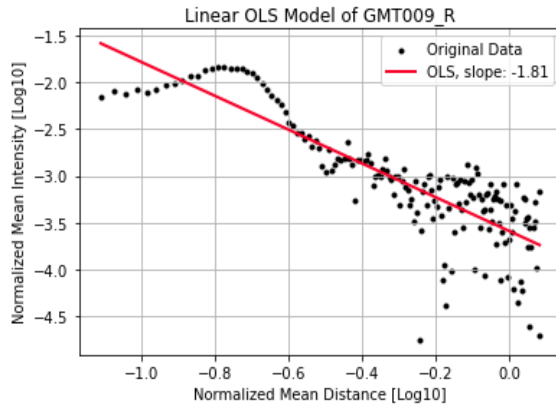
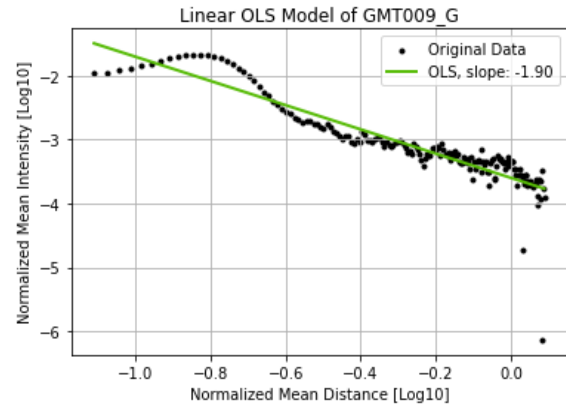


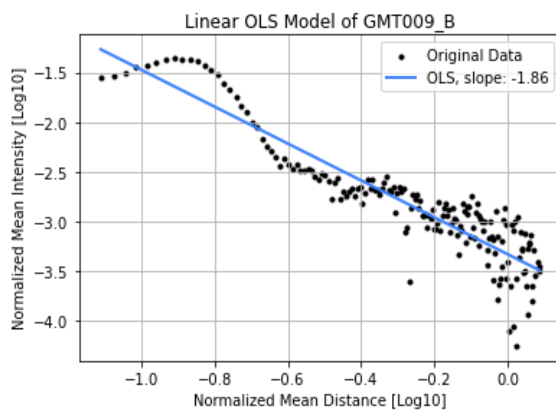
Figure B.6:



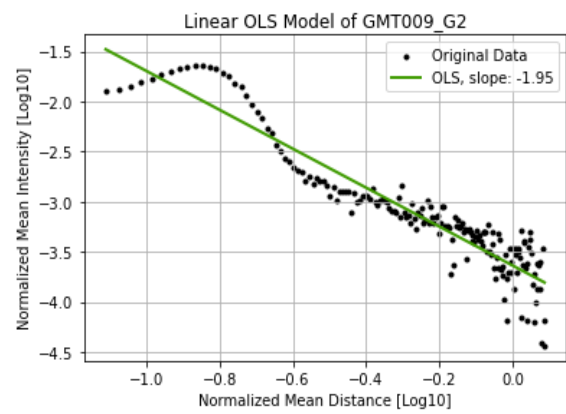
(a)



(b)

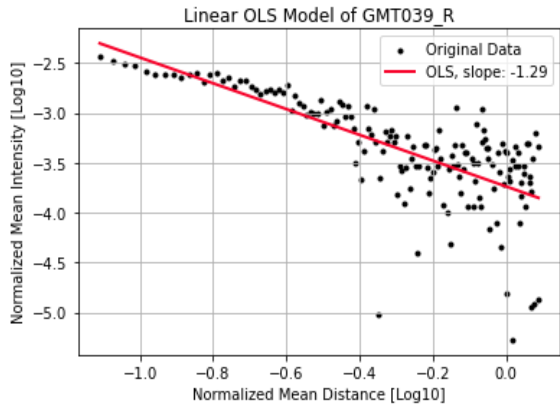


(c)

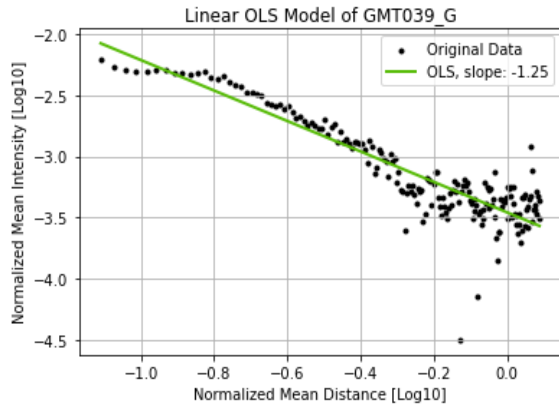


(d)

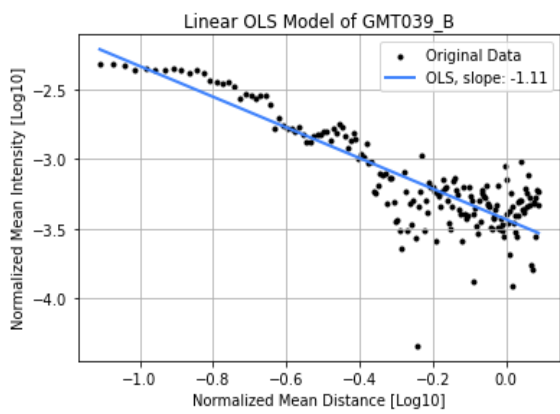
Figure B.7:



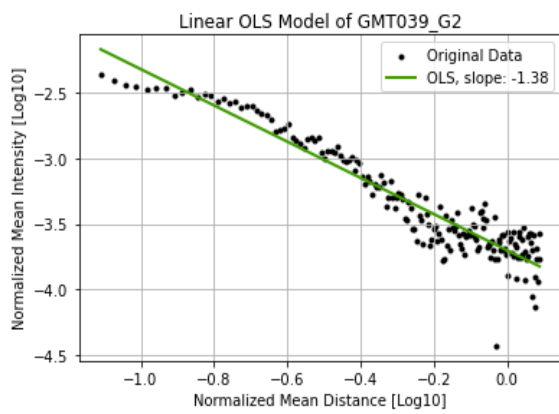
(a)



(b)

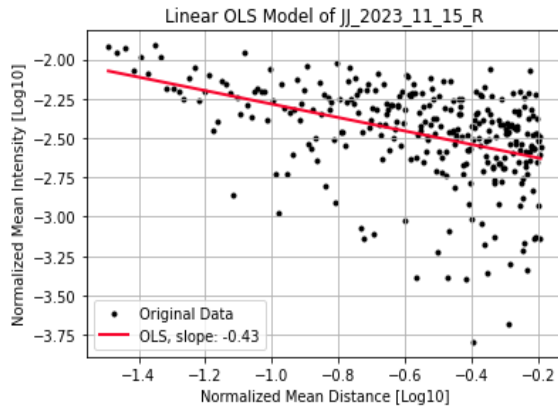


(c)

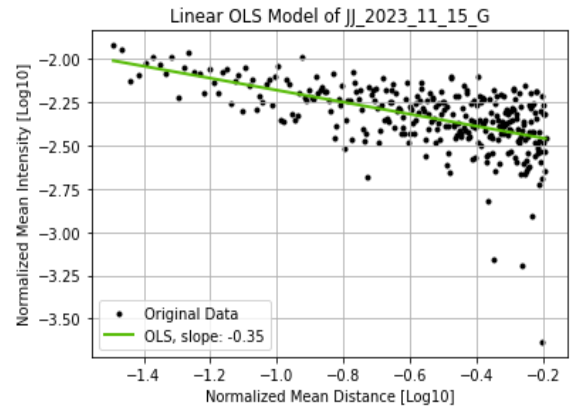


(d)

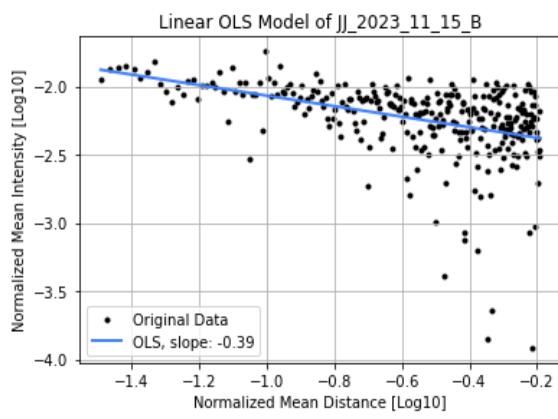
Figure B.8:



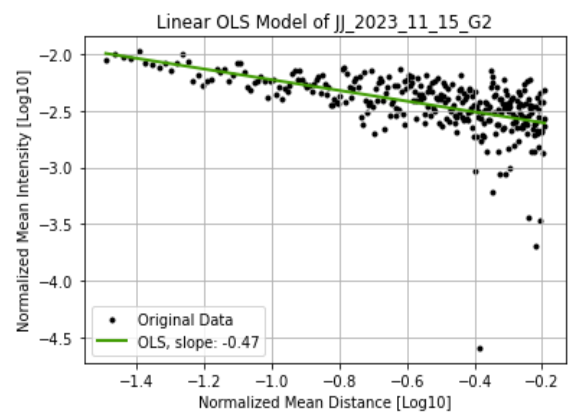
(a)



(b)

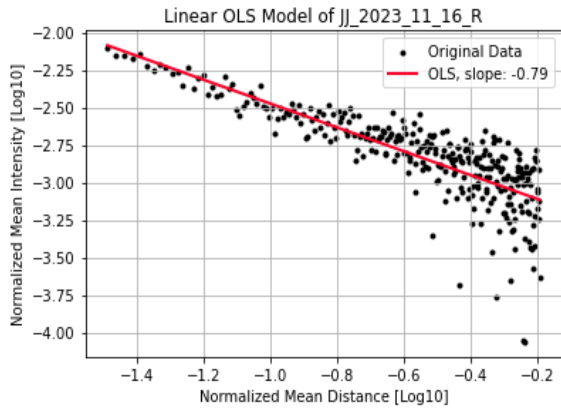


(c)

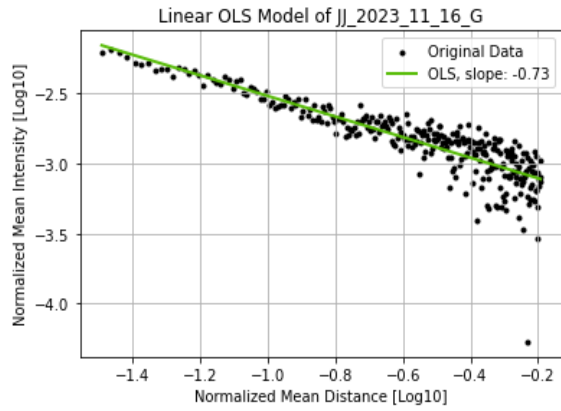


(d)

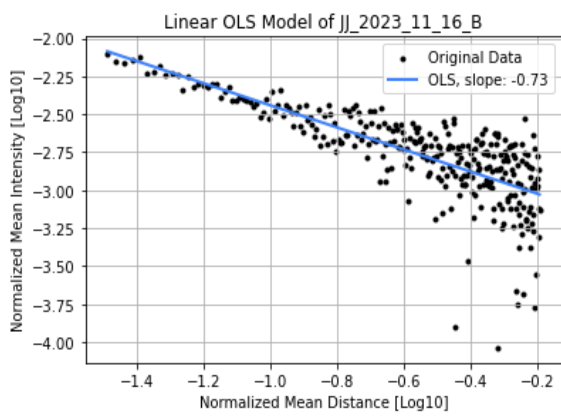
Figure B.9:



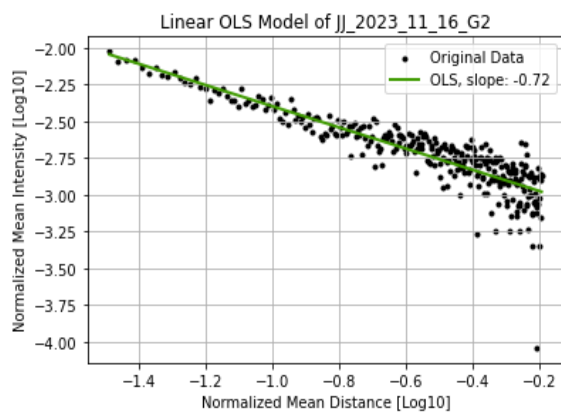
(a)



(b)



(c)



(d)

Figure B.10:

Technical
University of
Denmark

Elektrovej, building 327
2800 Kgs. Lyngby
Tlf. 4525 1700

<https://www.space.dtu.dk/english/>



Tidligere rapporter

Tidligere rapporter fra Danmarks Meteorologiske Institut kan findes på adressen:
<https://www.dmi.dk/publikationer/>